Pseudorapidity dependence of anisotropic flow and its decorrelations using long-range multiparticle correlations in Pb–Pb and Xe–Xe collisions

(Article begins on next page)

M.; Goswami, K.; Gotovac, S.; Grabski, V.; Graczykowski, L. K.; Grecka, E.; Grelli, A.; Grigoras, C.; Grigoriev, V.; Grigoryan, S.; Grosa, F.; Grosse-Oetringhaus, J. F.; Grosso, R.; Grund, D.; Guardiano, G. G.; Guernane, R.; Guilbaud, M.; Gulbrandsen, K.; Gundem, T.; Gunji, T.; Guo, W.; Gupta, A.; Gupta, R.; Gwizdziel, K.; Gyulai, L.; Hadjidakis, C.; Haider, F. U.; Hamagaki, H.; Hamdi, A.; Han, Y.; Hanley, B. G.; Hannigan, R.; Hansen, J.; Haque, M. R.; Harris, J. W.; Harton, A.; Hassan, H.; Hatzifotiadou, D.; Hauer, P.; Havener, L. B.; Heckel, S. T.; Hellbar, E.; Helstrup, H.; Hemmer, M.; Herman, T.; Herrera Corral, G.; Herrmann, F.; Herrmann, S.; Hetland, K. F.; Heybeck, B.; Hillemanns, H.; Hippolyte, B.; Hoffmann, F. W.; Hofman, B.; Hong, G. H.; Horst, M.; Horzyk, A.; Hou, Y.; Hristov, P.; Hughes, C.; Huhn, P.; Huhta, L. M.; Humanic, T. J.; Hutson, A.; Hutter, D.; Ilkaev, R.; Ilyas, H.; Inaba, M.; Innocenti, G. M.; Ippolitov, M.; Isakov, A.; Isidori, T.; Islam, M. S.; Ivanov, M.; Ivanov, V.; Iversen, K. E.; Jablonski, M.; Jacak, B.; Jacazio, N.; Jacobs, P. M.; Jadlovska, S.; Jadlovsky, J.; Jaelani, S.; Jahnke, C.; Jakubowska, M. J.; Janik, M. A.; Janson, T.; Ji, S.; Jia, S.; Jimenez, A. A. P.; Jonas, F.; Jones, D. M.; Jowett, J. M.; Jung, J.; Jung, M.; Junique, A.; Jusko, A.; Kabus, M. J.; Kaewjai, J.; Kalinak, P.; Kalteyer, A. S.; Kalweit, A.; Kaplin, V.; Karasu Uysal, A.; Karatovic, D.; Karavichev, O.; Karavicheva, T.; Karczmarczyk, P.; Karpechev, E.; Kebschull, U.; Keidel, R.; Keijdener, D. L. D.; Keil, M.; Ketzer, B.; Khade, S. S.; Khan, A. M.; Khan, S.; Khanzadeev, A.; Kharlov, Y.; Khatun, A.; Khuntia, A.; Kileng, B.; Kim, B.; Kim, C.; Kim, D. J.; Kim, E. J.; Kim, J.; Kim, J. S.; Kim, M.; Kim, S.; Kim, T.; Kimura, K.; Kirsch, S.; Kisel, I.; Kiselev, S.; Kisiel, A.; Kitowski, J. P.; Klay, J. L.; Klein, J.; Klein, S.; Klein-Bosing, C.; Kleiner, M.; Klemenz, T.; Kluge, A.; Knospe, A. G.; Kobdaj, C.; Kollegger, T.; Kondratyev, A.; Kondratyeva, N.; Kondratyuk, E.; Konig, J.; Konigstorfer, S. A.; Konopka, P. J.; Kornakov, G.; Korwieser, M.; Koryciak, S. D.; Kotliarov, A.; Kovalenko, V.; Kowalski, M.; Kozhuharov, V.; Kralik, I.; Kravcakova, A.; Krcal, L.; Krivda, M.; Krizek, F.; Krizkova Gajdosova, K.; Kroesen, M.; Kruger, M.; Krupova, D. M.; Kryshen, E.; Kucera, V.; Kuhn, C.; Kuijer, P. G.; Kumaoka, T.; Kumar, D.; Kumar, L.; Kumar, N.; Kumar, S.; Kundu, S.; Kurashvili, P.; Kurepin, A.; Kurepin, A. B.; Kuryakin, A.; Kushpil, S.; Kweon, M. J.; Kwon, Y.; La Pointe, S. L.; La Rocca, P.; Lakrathok, A.; Lamanna, M.; Landou, A. R.; Langoy, R.; Larionov, P.; Laudi, E.; Lautner, L.; Lavicka, R.; Lea, R.; Lee, H.; Legrand, I.; Legras, G.; Lehrbach, J.; Lelek, T. M.; Lemmon, R. C.; Leon Monzon, I.; Lesch, M. M.; Lesser, E. D.; Levai, P.; Li, X.; Li, X. L.; Lien, J.; Lietava, R.; Likmeta, I.; Lim, B.; Lim, S. H.; Lindenstruth, V.; Lindner, A.; Lippmann, C.; Liu, A.; Liu, D. H.; Liu, J.; Liveraro, G. S. S.; Lofnes, I. M.; Loizides, C.; Lokos, S.; Lomker, J.; Loncar, P.; Lopez, X.; Lopez Torres, E.; Lu, P.; Luhder, J. R.; Lunardon, M.; Luparello, G.; Ma, Y. G.; Mager, M.; Maire, A.; Majerz, E. M.; Makariev, M. V.; Malaev, M.; Malfattore, G.; Malik, N. M.; Malik, Q. W.; Malik, S. K.; Malinina, L.; Mallick, D.; Mallick, N.; Mandaglio, G.; Mandal, S. K.; Manko, V.; Manso, F.; Manzari, V.; Mao, Y.; Marcjan, R. W.; Margagliotti, G. V.; Margotti, A.; Marin, A.; Markert, C.; Martinengo, P.; Martinez, M. I.; Martinez Garcia, G.; Martins, M. P. P.; Masciocchi, S.; Masera, M.; Masoni, A.; Massacrier, L.; Massen, O.; Mastroserio, A.; Matonoha, O.; Mattiazzo, S.; Matuoka, P. F. T.; Matyja, A.; Mayer, C.; Mazuecos, A. L.; Mazzaschi, F.; Mazzilli, M.; Mdhluli, J. E.; Mechler, A. F.; Melikyan, Y.; Menchaca-Rocha, A.; Meninno, E.; Menon, A. S.; Meres, M.; Mhlanga, S.; Miake, Y.; Micheletti, L.; Migliorin, L. C.; Mihaylov, D. L.; Mikhaylov, K.; Mishra, A. N.; Miskowiec, D.; Modak, A.; Mohanty, A. P.; Mohanty, B.; Mohisin Khan, M.; Molander, M. A.; Monira, S.; Moravcova, Z.; Mordasini, C.; Moreira De Godoy, D. A.; Morozov, I.; Morsch, A.; Mrnjavac, T.; Muccifora, V.; Muhuri, S.; Mulligan, J. D.; Mulliri, A.; Munhoz, M. G.; Munzer, R. H.; Murakami, H.; Murray, S.; Musa, L.; Musinsky, J.; Myrcha, J. W.; Naik, B.; Nambrath, A. I.; Nandi, B. K.; Nania, R.; Nappi, E.; Nassirpour, A. F.; Nath, A.; Nattrass, C.; Naydenov, M. N.; Neagu, A.; Negru, A.; Nellen, L.; Nepeivoda, R.; Nese, S.; Neskovic, G.; Nicassio, N.; Nielsen, B. S.; Nielsen, E. G.; Nikolaev, S.; Nikulin, S.; Nikulin, V.; Noferini, F.; Noh, S.; Nomokonov, P.; Norman, J.; Novitzky, N.; Nowakowski, P.; Nyanin, A.; Nystrand, J.; Ogino, M.; Oh, S.; Ohlson, A.; Okorokov, V. A.; Oleniacz, J.; Oliveira Da Silva, A. C.; Oliver, M. H.; Onnerstad, A.; Oppedisano, C.; Ortiz Velasquez, A.; Otwinowski, J.; Oya, M.; Oyama, K.; Pachmayer, Y.; Padhan, S.; Pagano, D.; Paic, G.; Paisano-Guzman, S.; Palasciano, A.; Panebianco, S.; Park, H.; Park, J.; Parkkila, J. E.; Patley, Y.; Patra, R. N.; Paul, B.; Pei, H.; Peitzmann, T.; Peng, X.; Pennisi, M.; Perciballi, S.; Peresunko, D.; Perez, G. M.; Pestov, Y.; Petrov, V.; Petrovici, M.; Pezzi, R. P.; Piano, S.; Pikna, M.; Pillot, P.; Pinazza, O.; Pinsky, L.; Pinto, C.; Pisano, S.; Ploskon, M.; Planinic, M.; Pliquett, F.; Poghosyan, M. G.; Polichtchouk, B.; Politano', S.; Poljak, N.; Pop, A.; Porteboeuf-Houssais, S.; Pozdniakov, V.; Pozos, I. Y.; Pradhan, K. K.; Prasad, S. K.; Prasad, S.; Preghenella, R.; Prino, F.; Pruneau, C. A.; Pshenichnov, I.; Puccio, M.; Pucillo, S.; Pugelova, Z.; Qiu, S.; Quaglia, L.; Quishpe, R. E.; Ragoni, S.; Rai, A.; Rakotozafindrabe, A.; Ramello, L.; Rami, F.; Rancien, T. A.; Rasa, M.; Rasanen, S. S.; Rath, R.; Rauch, M. P.; Ravasenga, I.; Read, K. F.; Reckziegel, C.; Redelbach, A. R.; Redlich, K.; Reetz, C. A.; Regules-Medel, H. D.; Rehman, A.; Reidt, F.; Reme-Ness, H. A.; Rescakova, Z.; Reygers, K.; Riabov, A.; Riabov, V.; Ricci, R.; Richter, M.; Riedel, A. A.; Riegler, W.; Riffero, A. G.; Ristea, C.; Rodriguez, M. V.; Rodriguez Cahuantzi, M.; Rodriguez Ramirez, S. A.; Roed, K.; Rogalev, R.; Rogochaya, E.; Rogoschinski, T. S.; Rohr, D.; Rohrich, D.; Rojas, P. F.; Rojas Torres, S.; Rokita, P. S.; Romanenko, G.; Ronchetti, F.; Rosano, A.; Rosas, E. D.; Roslon, K.; Rossi, A.; Roy, A.; Roy, S.; Rubini, N.; Ruggiano, D.; Rui, R.; Russek, P. G.; Russo, R.; Rustamov, A.; Ryabinkin, E.; Ryabov, Y.; Rybicki, A.; Rytkonen, H.; Ryu, J.; Rzesa, W.; Saarimaki, O. A. M.; Sadhu, S.; Sadovsky, S.; Saetre, J.; Safarik, K.; Saha, P.; Saha, S. K.; Saha, S.; Sahoo, B.; Sahoo, R.; Sahoo, S.; Sahu, D.; Sahu, P. K.; Saini, J.; Sajdakova, K.; Sakai, S.; Salvan, M. P.; Sambyal, S.; Samitz, D.; Sanna, I.; Saramela, T. B.; Sarma, P.; Sarritzu, V.; Sarti, V. M.; Sas, M. H. P.; Schambach, J.; Scheid, H. S.; Schiaua, C.; Schicker, R.; Schmah, A.; Schmidt, C.; Schmidt, H. R.; Schmidt, M. O.; Schmidt, M.; Schmidt, N. V.; Schmier, A. R.; Schotter, R.; Schroter, A.; Schukraft, J.; Schweda, K.; Scioli, G.; Scomparin, E.; Seger, J. E.; Sekiguchi, Y.; Sekihata, D.; Selina, M.; Selyuzhenkov, I.; Senyukov, S.; Seo, J. J.; Serebryakov, D.; Serksnyte, L.; Sevcenco, A.; Shaba, T. J.; Shabetai, A.; Shahoyan, R.; Shangaraev, A.; Sharma, A.; Sharma, B.; Sharma, D.; Sharma, H.; Sharma, M.; Sharma, S.; Sharma, U.; Shatat, A.; Sheibani, O.; Shigaki, K.; Shimomura, M.; Shin, J.; Shirinkin, S.; Shou, Q.; Sibiriak, Y.; Siddhanta,

S.; Siemiarczuk, T.; Silva, T. F.; Silvermyr, D.; Simantathammakul, T.; Simeonov, R.; Singh, B.; Singh, K.; Singh, R.; Singh, S.; Singh, V. K.; Singhal, V.; Sinha, T.; Sitar, B.; Sitta, M.; Skaali, T. B.; Skorodumovs, G.; Slupecki, M.; Smirnov, N.; Snellings, R. J. M.; Solheim, E. H.; Song, J.; Songmoolnak, A.; Sonnabend, C.; Soramel, F.; Soto-hernandez, A. B.; Spijkers, R.; Sputowska, I.; Staa, J.; Stachel, J.; Stan, I.; Steffanic, P. J.; Stiefelmaier, S. F.; Stocco, D.; Storehaug, I.; Stratmann, P.; Strazzi, S.; Sturniolo, A.; Stylianidis, C. P.; Suaide, A. A. P.; Suire, C.; Sukhanov, M.; Suljic, M.; Sultanov, R.; Sumberia, V.; Sumowidagdo, S.; Swain, S.; Szarka, I.; Szymkowski, M.; Taghavi, S. F.; Taillepied, G.; Takahashi, J.; Tambave, G. J.; Tang, S.; Tang, Z.; Tapia Takaki, J. D.; Tapus, N.; Tarasovicova, L. A.; Tarzila, M. G.; Tassielli, G. F.; Tauro, A.; Tavira Garcia, A.; Tejeda Munoz, G.; Telesca, A.; Terlizzi, L.; Terrevoli, C.; Thakur, S.; Thomas, D.; Thoresen, F.; Tikhonov, A.; Timmins, A. R.; Tkacik, M.; Tkacik, T.; Toia, A.; Tokumoto, R.; Tomohiro, K.; Topilskaya, N.; Toppi, M.; Tork, T.; Torres, V. V.; Torres Ramos, A. G.; Trifiro, A.; Triolo, A. S.; Tripathy, S.; Tripathy, T.; Trogolo, S.; Trubnikov, V.; Trzaska, W. H.; Trzcinski, T. P.; Tumkin, A.; Turrisi, R.; Tveter, T. S.; Ullaland, K.; Ulukutlu, B.; Uras, A.; Usai, G. L.; Vala, M.; Valle, N.; Van Doremalen, L. V. R.; Van Leeuwen, M.; Van Veen, C. A.; Van Weelden, R. J. G.; Vande Vyvre, P.; Varga, D.; Varga, Z.; Vasileiou, M.; Vasiliev, A.; Vazquez Doce, O.; Vazquez Rueda, O.; Vechernin, V.; Vercellin, E.; Vergara Limon, S.; Verma, R.; Vermunt, L.; Vertesi, R.; Verweij, M.; Vickovic, L.; Vilakazi, Z.; Villalobos Baillie, O.; Villani, A.; Vino, G.; Vinogradov, A.; Virgili, T.; Virta, M. M. O.; Vislavicius, V.; Vodopyanov, A.; Volkel, B.; Volkl, M. A.; Voloshin, K.; Voloshin, S. A.; Volpe, G.; Von Haller, B.; Vorobyev, I.; Vozniuk, N.; Vrlakova, J.; Wan, J.; Wang, C.; Wang, D.; Wang, Y.; Wegrzynek, A.; Weiglhofer, F. T.; Wenzel, S. C.; Wessels, J. P.; Wiechula, J.; Wikne, J.; Wilk, G.; Wilkinson, J.; Willems, G. A.; Windelband, B.; Winn, M.; Wright, J. R.; Wu, W.; Wu, Y.; Xu, R.; Yadav, A.; Yadav, A. K.; Yalcin, S.; Yamaguchi, Y.; Yang, S.; Yano, S.; Yin, Z.; Yoo, I. -K.; Yoon, J. H.; Yu, H.; Yuan, S.; Yuncu, A.; Zaccolo, V.; Zampolli, C.; Zanone, F.; Zardoshti, N.; Zarochentsev, A.; Zavada, P.; Zaviyalov, N.; Zhalov, M.; Zhang, B.; Zhang, C.; Zhang, L.; Zhang, S.; Zhang, X.; Zhang, Y.; Zhang, Z.; Zhao, M.; Zherebchevskii, V.; Zhi, Y.; Zhou, D.; Zhou, Y.; Zhu, J.; Zhu, Y.; Zugravel, S. C.; Zurlo, N.. - In: PHYSICS LETTERS. SECTION B. - ISSN 0370-2693. - STAMPA. - 850:(2024), pp. 1-17. [10.1016/j.physletb.2024.138477]

PAPER • OPEN ACCESS

Pedestal evolution physics in low triangularity JET tokamak discharges with ITER-like wall

OPEN ACCESS
IOP Publishing | International Atomic Energy Agency
Nuclear Fusion
Nucl. Fusion **58** (2018) 016021 (17pp)
https://doi.org/10.1088/1741-4326/aa90bc

Pedestal evolution physics in low triangularity JET tokamak discharges with ITER-like wall

C. Bowman[1], D. Dickinson[1], L. Horvath[1,2], A.E. Lunniss[1], H.R. Wilson[1,2], I. Cziegler[1], L. Frassinetti[3], K. Gibson[1], A. Kirk[2], B. Lipschultz[1], C.F. Maggi[2], C.M. Roach[2], S. Saarelma[2], P.B. Snyder[4], A. Thornton[2], A. Wynn[1,2] and JET Contributors[a]

[1] York Plasma Institute, Department of Physics, University of York, Heslington, York YO10 5DD, United Kingdom
[2] CCFE, Culham Science Centre, Abingdon OX14 3DB, United Kingdom
[3] Association VR, Fusion Plasma Physics, KTH, SE-10044 Stockholm, Sweden
[4] General Atomics, PO Box 85608, San Diego, CA 92186-5608, United States of America

E-mail: howard.wilson@york.ac.uk

Received 9 June 2017, revised 10 September 2017
Accepted for publication 4 October 2017
Published 10 November 2017

Abstract

The pressure gradient of the high confinement pedestal region at the edge of tokamak plasmas rapidly collapses during plasma eruptions called edge localised modes (ELMs), and then re-builds over a longer time scale before the next ELM. The physics that controls the evolution of the JET pedestal between ELMs is analysed for 1.4 MA, 1.7 T, low triangularity, $\delta = 0.2$, discharges with the ITER-like wall, finding that the pressure gradient typically tracks the ideal magneto-hydrodynamic ballooning limit, consistent with a role for the kinetic ballooning mode. Furthermore, the pedestal width is often influenced by the region of plasma that has second stability access to the ballooning mode, which can explain its sometimes complex evolution between ELMs. A local gyrokinetic analysis of a second stable flux surface reveals stability to kinetic ballooning modes; global effects are expected to provide a destabilising mechanism and need to be retained in such second stable situations. As well as an electron-scale electron temperature gradient mode, ion scale instabilities associated with this flux surface include an electro-magnetic trapped electron branch and two electrostatic branches propagating in the ion direction, one with high radial wavenumber. In these second stability situations, the ELM is triggered by a peeling-ballooning mode; otherwise the pedestal is somewhat below the peeling-ballooning mode marginal stability boundary at ELM onset. In this latter situation, there is evidence that higher frequency ELMs are paced by an oscillation in the plasma, causing a crash in the pedestal before the peeling-ballooning boundary is reached. A model is proposed in which the oscillation is associated with hot plasma filaments that are pushed out towards the plasma edge by a ballooning mode, draining their free energy into the cooler plasma there, and then relaxing back to repeat the process. The results suggest

[a] See the author list of Litaudon X. *et al* 2017 *Nucl. Fusion* **57** 102001.

that avoiding the oscillation and maximising the region of plasma that has second stability access will lead to the highest pedestal heights and, therefore, best confinement—a key result for optimising the fusion performance of JET and future tokamaks, such as ITER.

Keywords: pedestal, ELMs, JET, stability

(Some figures may appear in colour only in the online journal)

1. Introduction

As the heating power in a tokamak plasma is gradually increased through a threshold, there is often a spontaneous transition from a low confinement state, called L-mode, to a high confinement state, called H-mode [1]. The improvement in confinement is a result of suppression of the turbulence in the few centimetres of plasma, just inside the last closed flux surface. This leads to a narrow region of steep pressure gradient at the plasma edge, called the pedestal region. The pressure in the core is approximately proportional to the pressure at the top of the pedestal (i.e. the top of the steep gradient region), so this so-called pedestal height has a major impact on the fusion performance of future tokamaks, like ITER, and the DT operation of JET.

Two properties influence the pedestal height—the gradient that the pedestal region supports and the width of that region. The EPED series of models [2, 3] have had considerable success in reproducing the experimentally measured pedestal heights over a very wide parameter set from multiple tokamaks, including JET. These models are built on the hypothesis that, while several mechanisms likely drive transport across the pedestal region, there are two modes that often play a primary role in providing the ultimate constraint on the evolution of the pedestal pressure profile. First there is a local 'soft' limit on the pedestal pressure gradient due to large transport induced by the kinetic ballooning mode (KBM), which is localised radially. Second, the pedestal width and gradient evolve (with gradient constrained by the KBM) until the coupled peeling-ballooning mode is triggered [4, 5], which causes an edge-localised mode (ELM) and the associated crash in the pedestal height that terminates the pedestal growth (or, in Quiescent H-mode, a quasi-stationary state with saturated mode). This peeling-ballooning mode is more global than the KBM, typically extending right across the pedestal and often somewhat into the core, so its onset condition is sensitive to both the width and the pressure gradient profile of the pedestal. These two constraints are sufficient to determine the pedestal height, width and average gradient, collectively referred to as the pedestal structure.

Calculating the stability and resulting turbulent transport associated with the KBM is a challenging, kinetic problem. The EPED series of models for the pedestal structure approach this challenge by employing simplified calculations, and analytic fits to these calculations, to derive a pedestal-averaged KBM constraint. Local gyrofluid and gyrokinetic calculations of KBM growth rates and transport indicate that the infinite toroidal mode number, n, ideal magneto-hydrodynamic (MHD) ballooning mode threshold provides a good approximation to the pressure gradient at which KBM growth rates and fluxes rise to large values [6]. Hence local ideal ballooning threshold calculations can in many cases be used as an accurate proxy for KBM onset. However, such local calculations indicate that the central region of the pedestal can in some cases become 'second stable'; that is, at sufficiently low magnetic shear the high n ballooning mode is stable for all pressure gradients. It is, however, known from finite (but large) n ideal MHD calculations that non-local effects can restrict this 'second stability' gap and lead to a finite pressure gradient limit, somewhat above the first stability limit [7]. There is also evidence from global gyrokinetic simulations that global effects close off the second stability region to KBMs [8]. The 'ballooning critical pedestal' technique used in EPED, employs high-n ideal MHD ballooning calculations and simple functional forms to provide an approximation to the average ballooning limit either with or without local regions of 2nd stability [3]. This leads to a scaling of the predicted pedestal width (in normalised flux) $\sim \beta_{\mathrm{p,ped}}^{1/2}$, where $\beta_{\mathrm{p,ped}}$ is a measure of the ratio of the thermal energy of the pedestal to the energy in the poloidal component of the magnetic field.

There is significant experimental evidence that indicates that the ELM-averaged pedestal width increases sub-linearly with $\beta_{\mathrm{p,ped}}$ [9–12], consistent with the above argument for the KBM constraint. In addition, a number of tokamaks, including MAST, NSTX, Alcator C-Mod and DIII-D, have found that the pedestal width, Δ_{ped}, increases as the pedestal height grows between ELMs at approximately fixed gradient [13, 14]. This is at least qualitatively consistent with the width growing as $\beta_{\mathrm{p,ped}}$ increases between ELMs (while recognising these parameters are closely coupled). In such cases, the stability threshold (eg in pressure gradient and/or current density) for the global peeling-ballooning mode falls as the pedestal widens between ELMs, ultimately triggering the instability and resulting in the ELM which terminates the pedestal growth. Detailed comparisons of the approach of the pedestal to the EPED constraints have been conducted on DIII-D and Alcator C-Mod, finding that the peeling-ballooning constraint is approached prior to the ELM, with the pressure gradient approximately clamped at the KBM critical value during the final evolution to the ELM [15–17].

Turning to JET, the EPED constraints give predictions for the pedestal height that agree with experiment to within $\pm 20\%$ [3, 18]. Also the variations of the JET pedestal structure with collisionality, normalised Larmor radius, ρ_* and normalised pressure, β_{N}, are found to be qualitatively consistent with the peeling-ballooning mode stability constraints [19]. However,

there are some trends that at first sight appear to be beyond the EPED model, such as the variation of pedestal height with strong gas puffing on JET [20] and the differences in pedestal structure between the carbon and ITER-like wall [18, 21], as well as the impact of impurity seeding [22]. Furthermore, it is not always the case that the calculated peeling-ballooning stability boundary is reached at the onset of the ELM [23], and it is often the case that the JET pedestal width reduces between ELMs [24], while the pedestal height, and therefore $\beta_{\mathrm{p,ped}}$, increases. The EPED model provides a prediction for the *pressure* pedestal structure and must take the relative contributions of the density and temperature pedestal profiles as inputs; these are known to influence stability (and therefore the EPED prediction—see [25] and references therein). Indeed, the variation of the ASDEX Upgrade pedestal structure with fueling and impurity seeding can be understood in terms of the KBM and peeling-ballooning constraints when the experimentally observed variations in the locations of the density and temperature pedestals are taken into account as inputs to the model [25]—thus, while this effect is beyond the *predictive* capability of EPED, it is not inconsistent with the physics that underlies it. To understand whether or not the above-mentioned trends of the JET pedestal are consistent with peeling-ballooning and KBM constraints requires a detailed understanding of how the pedestal parameters evolve with varying conditions, and then how the pedestal stability depends on those parameters.

The goal of this paper is to develop an improved understanding of the physics that influences the evolution of the JET pedestal between ELMs. This may then help us to identify how to maximise the pedestal height, and so optimise confinement. Specifically, we focus on a detailed pedestal stability analysis of representative discharges to explore the two aspects that underpin the EPED models, and see if we can understand some of the JET pedestal characteristics. First, we employ the infinite toroidal mode number, n, ideal MHD ballooning mode proxy for the KBM, and explore whether there is evidence that the pressure gradient is locally clamped at this stability boundary during the evolution between ELMs. This proxy has been shown to work well for JET when the plasma is constrained by the first ballooning stability boundary [24] but, as mentioned above, the situation is more complex when the plasma has $n = \infty$ ideal ballooning second stability access. We therefore also perform a local gyrokinetic stability analysis of a second-stable JET pedestal to explore the microinstabilities that exist. Second, we test whether the pedestal evolves towards the peeling-ballooning boundary as the ELM onset is approached, and shed new light on the ELM trigger physics in peeling-ballooning stable situations.

The paper is set out as follows. In the following section, we describe the data set and how it is analysed. Then, in section 3, we calculate how the pedestal stability evolves between ELMs, and test whether it is consistent with the physics that underpins the EPED model. We then study the ELM characteristics in section 4, comparing situations where the plasma does reach the peeling-ballooning boundary with those where it does not. We close in section 5 with conclusions and suggestions for further research.

2. Data set

The data we consider are taken from power and gas-puff scans in the JET tokamak with the ITER-like wall (JET-ILW), operated at fixed magnetic field, 1.7 T, and current, 1.4 MA. We focus on low triangularity, $\delta = 0.2$, discharges. This data set is described in more detail in [23]; here we provide a brief overview for completeness.

Fuelling is provided by three different levels of gas puffing: 2.8, 8.4 and 18 $\times$ 10^{21} e s^{-1} (low, medium and high), while the heating power is also varied to provide a range of β_{N}, which is the normalised plasma pressure. For the low gas puff power scan, the divertor strike points were close to the corners and β_{N} was varied from ~1.5 up to ~3, while for the high gas puff scan the outer strike point was on the horizontal target (tile 5) and the variation in β_{N} was from ~1 to ~2. Plasma density and temperature profiles are reconstructed from high resolution Thomson scattering (HRTS) by averaging over multiple ELM cycles, binning the data according to the timing of the HRTS laser pulse relative to the next ELM: 0–20%, 20–40%, 40–60%, 60–80% and 80–99% of the ELM cycle [26]. The ion temperature is assumed to be equal to the electron temperature. We ignore the first period, 0–20%, as it is likely affected by the physics of the previous ELM crash, and perform four mtanh fits to the set of profiles in each of the remaining time windows. Four high resolution equilibria are reconstructed by solving the Grad–Shafranov equation using the resulting profile fits; these serve as a basis for the stability analyses.

A previous pedestal stability study [23] focused on profiles taken from averages over the last 30% of the ELM cycle. In that work, an ideal MHD stability analysis showed that for the low gas puff scenarios, the peeling-ballooning mode is marginally stable, and therefore consistent with the ELM trigger. However, for high gas puff scenarios, the peeling-ballooning mode stability boundary is typically not reached at the ELM onset (except at low β_{N}), suggesting that it alone cannot explain the ELM trigger in these discharges. Our aim in this paper is to study the time evolution of the pedestal structure between ELMs to understand how it approaches the ELM trigger and what is the dominant physics that underlies JET pedestal dynamics.

3. Pedestal stability study

We have analysed the evolution of the pedestal height and width for eleven $\delta = 0.2$ discharges that span the range of gas puff and β_{N} discussed in section 2, comparing these to the marginal stability boundary for the peeling-ballooning mode (evaluated using ELITE [27, 28] for the equilibria constructed from the 80–99% time window) [29] (see appendix for more details on the methodology). We find four different kinds of behaviour, with examples of each shown in figures 1(*a*)–(*d*):

1. The pedestal width is approximately constant (perhaps broadening slightly) as the ELM is approached, and the peeling-ballooning boundary is reached at the ELM onset—figure 1(*a*): low gas puff, $\beta_{\mathrm{N}} = 1.3$.

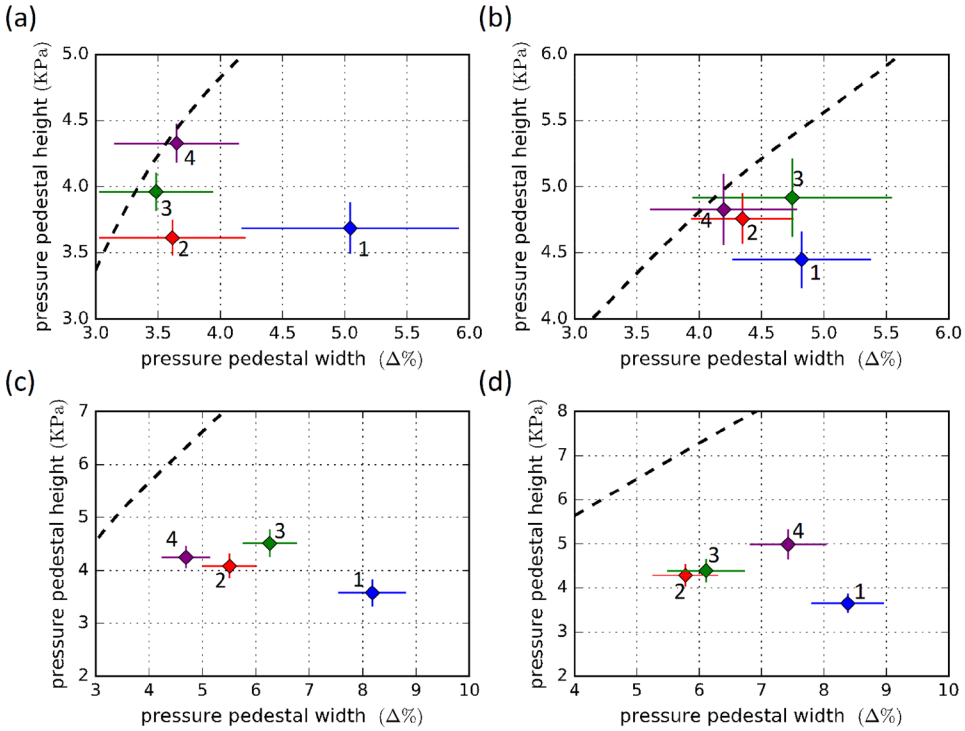

Figure 1. Evolution of pedestal height and width for JET discharges (a) 84797, (b) 84795, (c) 87350 and (d) 87342 (1: 20–40% blue diamond; 2: 40–60% red diamond; 3: 60–80% green diamond; 4: 80–99% purple diamond). The curve shows the peeling-ballooning boundary evaluated for the 80–99% period. (*a*) and (*b*) are low gas puff, while (*c*) and (*d*) are high gas puff.

2. The pedestal width evolution between ELMs has no clear trend, but the peeling-ballooning boundary is reached at the ELM onset—figure 1(*b*): low gas puff, $\beta_N = 1.7$.
3. The pedestal width evolution between ELMs has no clear trend, and the peeling-ballooning boundary is not reached at the ELM onset—figure 1(*c*): high gas puff, $\beta_N = 1.7$.
4. The pedestal width shows signs of broadening as the ELM is approached, but the peeling ballooning boundary is not reached at the ELM onset—figure 1(*d*): high gas puff, $\beta_N = 1.9$.

We study representative examples for each of these cases in this section.

3.1. Peeling-ballooning constraint

Figure 1(*a*) shows the evolution of pedestal width and height between ELMs for discharge 84797, which has low gas puff and low $\beta_N = 1.3$. We see that the peeling-ballooning boundary is reached at the onset for the ELM, as is typically the case for low gas puff in JET-ILW [23]. The pedestal width first reduces as it recovers from the previous ELM and then, within error bars, is consistent with being approximately constant as the ELM is approached—perhaps slightly increasing. The EPED assumption that the peeling-ballooning mode is triggered at the ELM onset is therefore satisfied in this case. Figure 1(*b*) is for discharge 84795, which is again low gas puff, but a higher $\beta_N = 1.7$. Again we see that the discharge is peeling-ballooning limited at the time of ELM onset, but there is no clear trend in the pedestal width and, if anything, it is decreasing as the ELM is approached, while the pedestal height (and therefore $\beta_{p,ped}$) remains approximately constant. Figure 1(*c*) is for discharge 87350, which has the same $\beta_N = 1.7$ as figure 1(*b*), but at high gas puff. Again we observe a falling pedestal width as the ELM is approached, but this time the discharge is clearly well short of the peeling-ballooning boundary at the time the ELM is triggered. Finally, figure 1(*d*) is for discharge 87342 which also has high gas puff but a slightly higher $\beta_N = 1.9$. For this case, the pedestal width broadens towards the ELM onset, but the peeling ballooning boundary is again not reached.

In summary, we find that the peeling-ballooning boundary is typically reached in JET-ILW discharges when there is low gas puff, but at higher gas puff the pedestal is often far from this boundary (except at the lowest β_N), suggesting that additional physics is required to explain the ELM onset in these cases. This is consistent with earlier results presented in [23] which provide a more detailed analysis of the peeling-ballooning stability close to the time of ELM onset, including their position relative to the stability boundary plotted in terms of current density and pressure gradient. Specifically, figure 9(*b*) of [23] shows discharge 87341 (medium gas puff, $\beta_N = 2$), which only approaches second stable access close to ELM onset and does not reach the peeling-ballooning boundary; figure 11(*a*) of [23] shows discharge 84794 (low gas puff, $\beta_N = 2.76$) which has second stability access throughout most of the ELM cycle and does reach the peeling ballooning boundary. Finally, we note that there is no clear, consistent relationship between the inter-ELM evolution of the pedestal width and $\beta_{p,ped}$ (which is proportional to the pedestal height).

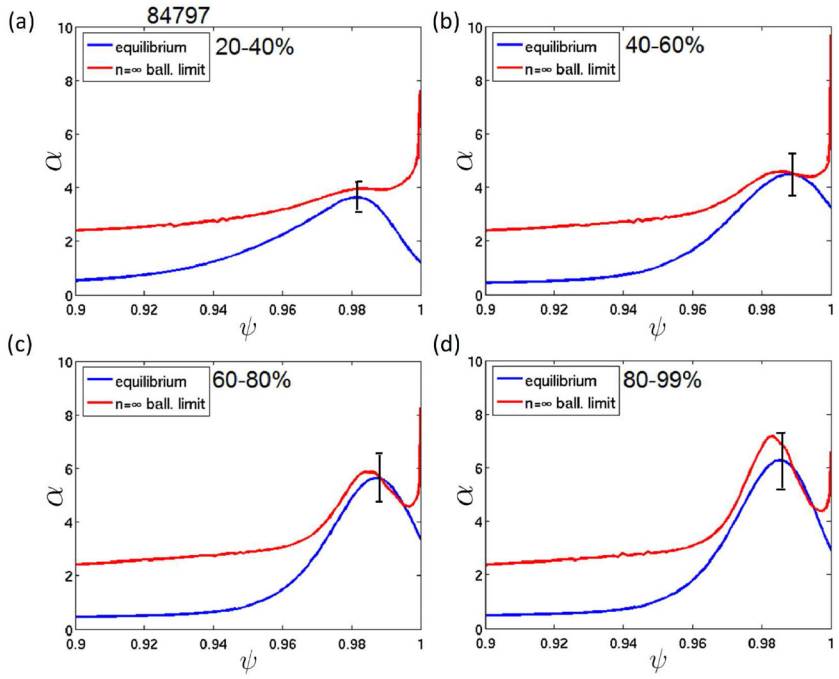

Figure 2. Comparison of the measured edge pressure gradient profile (blue, lower curve) with the ideal MHD ballooning limit (red, upper curve) as a function of normalised flux for JET-ILW discharge 84797 for each time window: (a) 20–40%, (b) 40–60%, (c) 60–80% and (d) 80–99%. ψ is the poloidal flux, normalised to $\psi = 1$ at the separatrix. The vertical line is the 1σ error bar in the measured value of the maximum α.

3.2. KBM constraint

We now turn to consider the KBM constraint in a little more detail, and address the question of whether the local pedestal gradient is limited by this mode. Saarelma *et al* [24] studied this in two high triangularity discharges in JET with the carbon wall, JET-C. In particular, they generally found good agreement between the threshold pressure gradient predicted by the infinite-n ideal MHD ballooning mode and the KBM threshold evaluated using the local gyrokinetic code, GS2. For this study, our main focus is therefore on comparing the measured pedestal pressure gradient with the local ideal ballooning threshold, assumed to be a reliable proxy for the onset of the KBM.

3.2.1. Low gas puff discharges. Figure 2 compares the measured profile of the normalised pressure gradient, α, with the calculated threshold for ideal MHD ballooning modes for the discharge 84797 (figure 1(*a*)). This threshold is calculated using HELENA [30], which scales the pressure gradient (α) coefficient of the curvature drive until marginal stability is reached—the threshold is this scaled value of α, and is accurate provided the equilibrium is close to marginal stability (we return to this important issue below). Recall that this discharge does reach the peeling-ballooning mode boundary at ELM onset. Note the region of higher α in the range $0.96 < \psi < 1$, which corresponds to the edge transport barrier of the pedestal region. It is remarkable how closely the measured pedestal pressure gradient tracks the theoretical threshold as it evolves, the threshold increasing by almost a factor of 2 between ELMs. Finally the pressure gradient is sufficient to drive the peeling-ballooning mode, triggering the ELM and collapse of the pedestal, for the cycle to then repeat. In this case we have good quantitative agreement with the two physics hypotheses underpinning EPED—the local pedestal gradient is constrained by KBMs, and the pedestal evolution is terminated by the onset of a global peeling-ballooning mode in the 80–99% window, triggering an ELM. A key point is that while this provides strong evidence that the pedestal evolution is constrained by the KBM, this is not a constant pressure gradient constraint—the threshold increases through the ELM cycle. We shall return to consider this in more detail shortly.

The error bar in α is calculated by first using the fits to the Thomson data for electron density and temperature to derive the uncertainties in the pedestal parameters (width, height, slope, etc). Thousands of calculations of pressure gradient were then derived, generated by Monte Carlo with a Gaussian distribution in the parameters that contains the calculated uncertainty. This provides a distribution of pressure gradients, and the error bar provided is the 1σ width of that distribution.

We now proceed to consider discharge 84795, which was also at the peeling-ballooning limit at the time of the ELM crash, but the pedestal width evolution is more complex (see figure 1(*b*)). Figure 3 compares the measured edge pressure gradient profile with the ideal MHD ballooning limit. We see it is very similar to discharge 84797, which also hit the peeling-ballooning limit, but the ballooning threshold starts to increase in the pedestal somewhat earlier in the cycle, allowing the pressure gradient to also increase earlier. Again, the pressure gradient tracks the threshold throughout, only lagging behind in the last time phase when the threshold increases very rapidly. Therefore, despite the somewhat complex width evolution, the pedestal dynamics are again consistent with the physics that underpins the EPED model—the

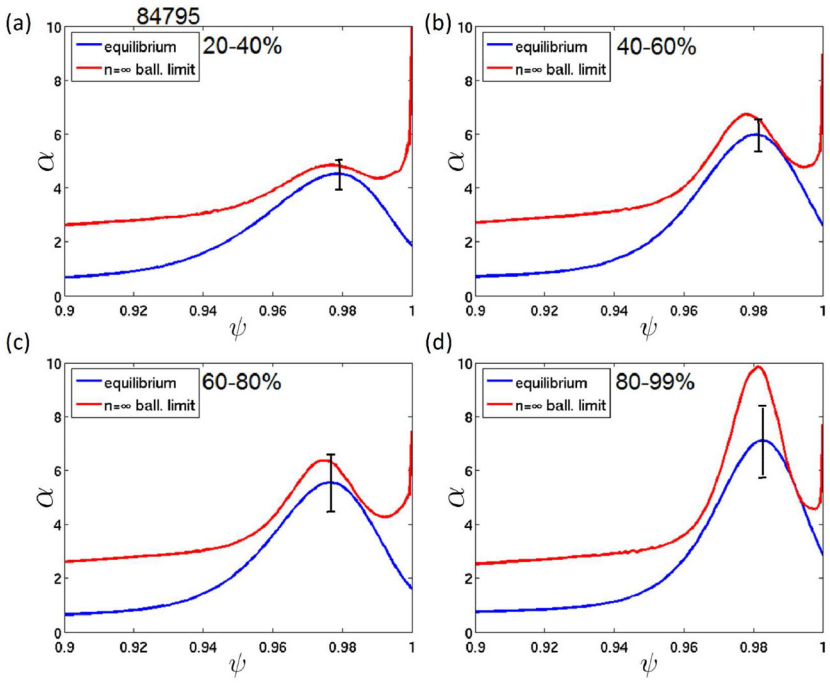

Figure 3. Comparison of the measured edge pressure gradient profile (blue, lower curve) with the ideal MHD ballooning limit (red, upper curve) as a function of normalised flux for JET-ILW discharge 84795 for each time window: (a) 20–40%, (b) 40–60%, (c) 60–80% and (d) 80–99%. The vertical line is the 1σ error bar in the measured value of the maximum α.

ELM is triggered by the peeling-ballooning mode and the gradient tracks the ideal MHD ballooning limit as it increases, except in the final time window when the threshold increases rapidly. We will now explore why the threshold is increasing so strongly.

In a simple model, one might assume the KBM clamps the pressure gradient at a fixed threshold. Figures 2 and 3 show that this is not always the case, and in fact the threshold pressure gradient can rise significantly between ELMs. To understand this, we show in figure 4 the ideal ballooning stability using so-called s-α plots, where s is the magnetic shear, which decreases with increasing current density. We analyse for discharge 84795 the surface $\psi = 0.98$, which is close to the maximum in the pressure gradient, and show in figure 4 the results for each of the four inter-ELM time slices. Note that these figures illustrate a regime of stability at low pressure gradient, the first stability region, and then a second region of stability at higher pressure gradient. The two stable regions connect at sufficiently low shear, i.e. sufficient current density, providing the possibility of access to the second stability region. These features are highlighted in figure 4(a). The width of this region of 'second stable access' (i.e. how much current density is required to access it) depends on a number of factors in separatrix geometry, including shape, poloidal β and safety factor [31]. The marginal stability contours in the s-α plots are derived by modifying the equilibrium and ballooning stability in a self-consistent way as s and α are varied, retaining the impact on local shear [31]; for HELENA the curvature drive in the ballooning equation is simply scaled until marginal stability is found, without retaining the modifications to the equilibrium and, specifically, does not take account of the modification to local shear. Both approaches are meaningful estimates when the equilibrium is close to marginal stability and therefore α requires little scaling to reach the stability boundary. However, because the HELENA approach does not include the impact of varying α on local shear it can lead to unphysical stability boundaries when the equilibrium is far from marginal stability (and hence requires significant scaling of α). In particular, local shear is key to second stability, which is why figures 3(b)–(d) indicate an unphysical threshold at $\psi = 0.98$, while the associated s-α plots of figures 4(b)–(d) show the plasma to be clearly in the second stable regime, with no threshold in α.

In the early phase of the cycle, figure 4(a), the plasma does not have sufficient current density to access the second stability regime, so the pressure gradient is clamped at a low level—the first stability boundary. However, later on, figures 4(b) and (c), perhaps as the current starts to build on a current diffusion timescale, the shear is reduced, and the equilibrium starts to get into the second stable access region, where the threshold α increases rapidly for a small decrease in magnetic shear (i.e. small increase in current density). The current density in the pedestal is dominated by the bootstrap current, which is proportional to the pressure gradient, but also depends on collisionality, with low collisionality plasmas having higher bootstrap current density. On the other hand, the current density can only grow on a current diffusion time—if this is longer than the energy diffusion time that the pressure gradient grows on (i.e. at high temperatures where the resistivity is low) then the current density will lag behind its bootstrap value. Thus, the dynamics of how s and α vary relative to each other between ELMs, and therefore whether one has access to second stability, is likely subtle and depends on the transport processes as well as equilibrium plasma parameters.

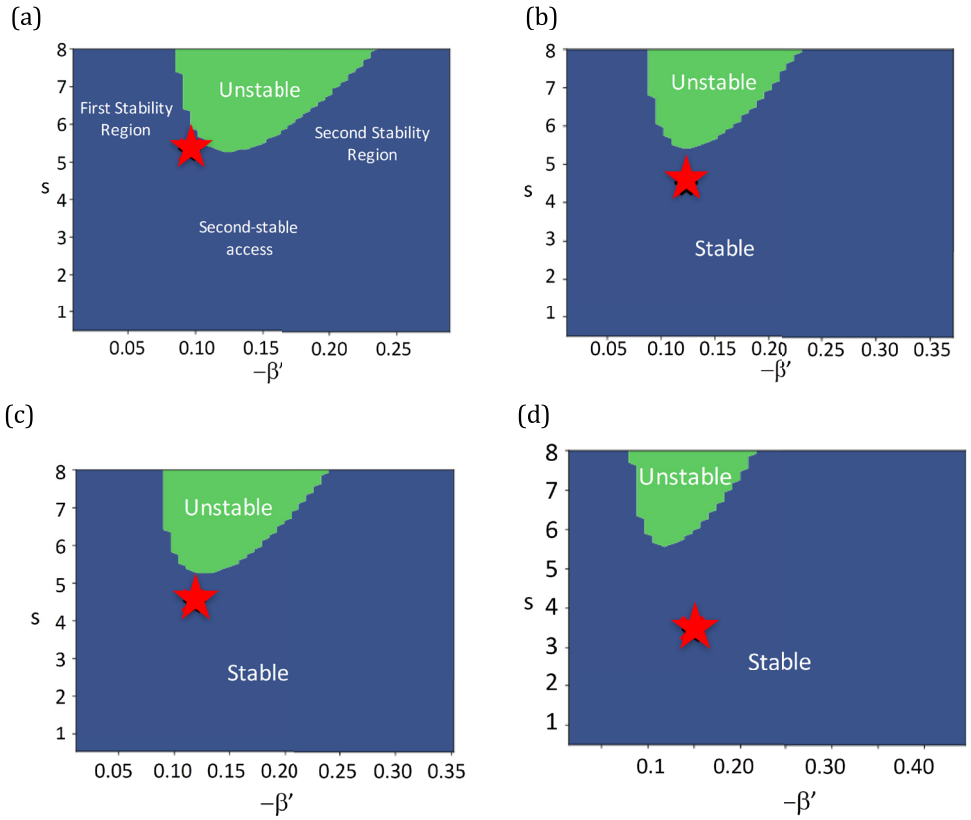

Figure 4. s-α diagrams for the $\psi = 0.98$ surface of discharge 84795 for (a) the 20–40% time window; (b) the 40–60% time window; (c) the 60–80% time window, and (d) the 80–99% window (note, β' is proportional to the normalised pressure gradient parameter, α). The red star denotes the equilibrium parameters.

In our calculation we have assumed the current density is the fully penetrated bootstrap current.

It is worth commenting on the impact of the error in α. Because the threshold (red curve in figures 2 and 3) depends on the local bootstrap current density, which in turn depends on pressure gradient, it will also have an error bar. Specifically, if the true pressure gradient were at the upper end of its error bar, then the current density would be higher than we have used for the threshold calculation, the plasma would be deeper in second stability and the HELENA prediction for the threshold would be higher (in such plasmas in close proximity to the second stability regime). Thus there is a robustness of the relative positions of the experimental pressure gradient and the threshold to uncertainties in the pressure gradient.

We can now start to understand the complex behaviour of the pedestal width evolution. On several tokamaks, this width is observed to expand monotonically throughout the inter-ELM period at fixed gradient [13, 14]. There is some evidence that micro-tearing modes may play a role in the dynamics [13, 24, 32], but a complete understanding of the physics that controls the width evolution is not yet available. In these JET discharges, the steepest gradient region which defines the pedestal is that part which has access to second stability. Therefore, the pedestal width evolution is determined at least to some extent by the width of the region that has second stable access—if this is narrow, the pedestal width will narrow as it pushes up into second stability during the latter part of the ELM cycle. This width of second stable access is strongly influenced by shaping and the amount of bootstrap current density flowing for a given pressure gradient, leading to possible dependencies on collisionality and resistivity (e.g. impurity species).

As the plasma starts to enter the second stable access region, the KBM threshold rises and we see that the equilibrium gradient tracks it closely at first, providing strong evidence for the KBM constraint on the pressure gradient. However, once the plasma is deeply into the second stable access region, the infinite n ideal ballooning proxy predicts no threshold to the KBM. It is possible that other micro-instabilities play an important role determining the gradient in this situation, such as microtearing modes and electron temperature gradient (ETG) driven modes [33], or that kinetic effects can destabilise the KBM relative to the ideal ballooning mode in such second stable access regimes. Another possibility is that global effects associated with finite (but large) n KBMs cause a coupling to the kink mode that restricts the second stable access, as found in global ideal MHD calculations [7, 28]. The coupling to the kink mode cannot be tested with gyrokinetic codes, as the necessary terms are formally O(1/n), and are ordered out of the standard gyrokinetic theory. Nevertheless, they can be important when the current density gradient is large, as is the case for a second-stable pedestal with strong bootstrap current [29]. It is interesting to note that global simulations (without the kink drive) of the KBM do indicate they can be unstable

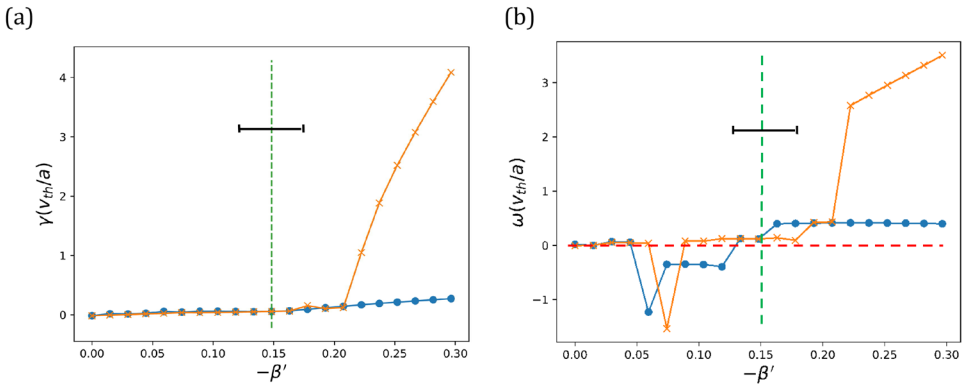

Figure 5. (*a*) Growth rate γ and (*b*) mode frequency ω from a local solution to the gyrokinetic equation provided by the GS2 code for the 80–99% window of discharge 84795 at $\psi = 0.98$, which is in the ideal ballooning second stability region (corresponding to figure 4(*d*)). We have fixed $k_y\rho_s = 0.1$ (i.e. $n = 24$), and $\omega < 0$ corresponds to propagation in the electron diamagnetic direction. The vertical dashed line denotes the equilibrium value of normalised pressure gradient, β', about which we perturb by increasing density and temperature gradients at the same rate (i.e. fixed $\eta_{i,e}$). The blue curve with full circles shows the result for self-consistently modifying the local equilibrium, while the yellow curve with crosses shows the result when the equilibrium is not adjusted with β'; γ and ω are normalised to v_{th}/a (v_{th} is the thermal velocity and a the minor radius). The horizontal bar is the 1σ error in the experimental value of β'.

when local calculations indicate second stability [8], so it is likely that they will play an important role in pedestal transport even in second stable plasmas.

To explore a possible role for *local* kinetic instabilities in discharge 84795 at $\psi = 0.98$ just before the ELM where the pedestal is deep in the second stability region (corresponding to figure 4(*d*)), we have performed some local linear gyrokinetic stability calculations using GS2 [34]. As expected from our ideal ballooning analysis, and as found in [24], the conventional KBM (which propagates in the ion diamagnetic drift direction) is found to be stable within such a local analysis. We have identified three other ion-scale instabilities all with comparable growth rates and all with twisting parity:

(1) One which propagates in the electron diamagnetic drift direction with features of the hybrid trapped-electron/kinetic ballooning mode (hybrid TEM/KBM) identified in [35], having a growth rate that is sensitive to the parallel component of the magnetic field fluctuations and collision frequency.
(2) An electrostatic mode that propagates in the ion direction.
(3) A second electrostatic mode which propagates in the ion direction but with an unusually large radial wavenumber.

We also find an instability at electron scales which has features of the ETG mode. While simple mixing length estimates suggest the transport would be dominated by the ion scale instabilities, it is necessary to perform non-linear simulations and retain flow shear in order to make a definitive statement about their relative transport contributions.

The different ion scale modes mentioned above have been identified by performing scans in the pressure gradient parameter β', scaling the (logarithmic) density and temperature gradients to enhance β', but keeping their ratio, $\eta_{i,e}$, fixed for both ions and electrons. The results from two approaches are shown in figure 5: one where the local equilibrium is adjusted self-consistently (blue curve, circle symbols), and one where only the local instability drive is modified (similar to the HELENA approach for ideal ballooning modes). We have chosen $k_y\rho_s = 0.1$, (i.e. $n = 24$) where k_y is the poloidal mode number and ρ_s is the sound speed ion Larmor radius—the results for other $k_y\rho_s$ values are qualitatively similar. Below the equilibrium value of β', denoted by the vertical dashed line in figure 5, we see flipping between modes (1) and (2)—these modes have very similar growth rates, but propagate in opposite directions (GS2 reveals the most unstable mode for given plasma parameters). As we increase β' above the equilibrium value, adjusting the equilibrium in a self-consistent way (as for the s-α plots of figure 4), there is a modest increase in the growth rate and a new dominant mode emerges, propagating in the ion direction (blue curve, closed circle symbols of figure 5). While the direction of propagation is consistent with the KBM, there are three features that suggest it is not this mode: (1) we find an increase in its growth rate when magnetic fluctuations are switched off, while the KBM is electromagnetic; (2) the frequency is independent of β' while the KBM mode frequency is expected to follow the ion diamagnetic frequency (i.e. proportional to β'), and (3) there is no dramatic rise in growth rate beyond a threshold as expected for the KBM. Furthermore, the ballooning eigenfunction for this mode has a large radial wavenumber (the ballooning angle, $\theta_0 > 2\pi$). In contrast, the inconsistent scan, increasing only the instability drive, (yellow curve, cross symbols of figure 5) reveals both the strong increase in growth rate and a frequency proportional to β' above a threshold in the region of $|\beta'| = 0.21$—classic signatures of the KBM. The conclusion is that according to the local theory, the KBM is stable in the second stable region of this discharge, and reliable KBM stability calculations likely require gobal effects to be retained.

We have also searched for micro-tearing modes, varying the ratio of logarithmic derivatives of temperature to density gradients at the equilibrium pressure gradient, but found no evidence to support a significant role for them in the pedestal dynamics at this position in the pedestal where the pressure gradient is a maximum.

To summarise the results for these two low gas puff discharges, we have shown that the pedestal evolves to a

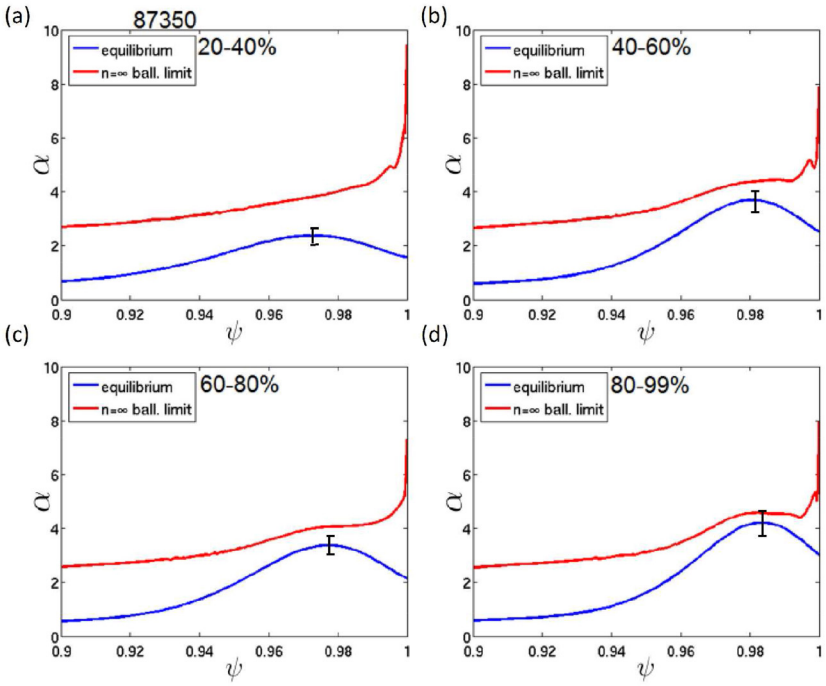

Figure 6. Comparison of the measured edge pressure gradient profile (blue, lower curve) with the ideal MHD ballooning limit (red, upper curve) as a function of normalised flux for JET-ILW discharge 87350 for each time window: (a) 20–40%, (b) 40–60%, (c) 60–80% and (d) 80–99%. ψ is the poloidal flux, normalised to $\psi = 1$ at the separatrix. The vertical line is the 1σ error bar in the measured value of the maximum α.

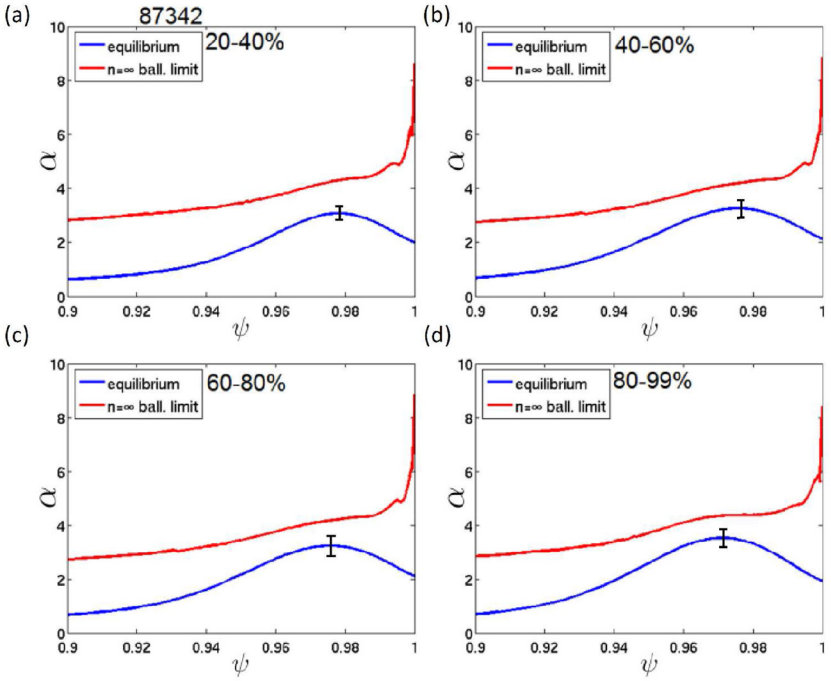

Figure 7. Comparison of the measured edge pressure gradient profile (blue, lower curve) with the ideal MHD ballooning limit (red, upper curve) as a function of normalised flux for JET-ILW discharge 87342 for each time window: (a) 20–40%, (b) 40–60%, (c) 60–80% and (d) 80–99%. ψ is the poloidal flux, normalised to $\psi = 1$ at the separatrix. The vertical line is the 1σ error bar in the measured value of the maximum α.

second-stable final state at the ELM onset consistent with KBM constraining the local pressure gradient through much of the ELM cycle and peeling-ballooning modes terminating the evolution in an ELM crash. Thus the physics is consistent with that which motivates the EPED model, but the dynamics controlled by the KBM can be more complex than a widening pedestal at fixed gradient, especially for these plasmas with second stability access.

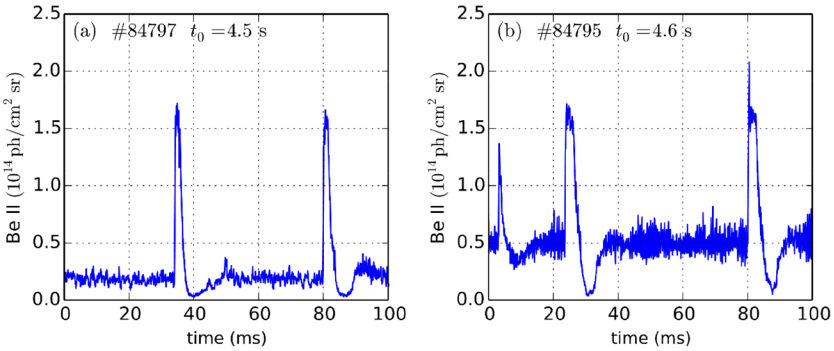

Figure 8. Emission of Be II from the inner divertor, starting at time t_0, showing the ELMs in the low gas puff discharges (*a*) 84797 and (*b*) 84795, which do reach the peeling-ballooning boundary at the ELM onset time.

3.2.2. High gas puff discharges. Let us now turn to consider the high gas puff discharges that do not reach the peeling-ballooning stability limit. In figure 6 we show how the measured pressure gradient profile compares with the ballooning stability threshold for discharge 87350, which has the same $\beta_N = 1.7$ as the low gas puff discharge 84795. We see that in this case the pressure gradient is again constrained just below the ideal ballooning boundary, indicating that the KBM is playing a key role, particularly as the ELM is approached. However, there is no time when the threshold pressure gradient rises sharply, although there is just the first sign of a slight increase in the final time window. This indicates that the pedestal does not have second stability access in this higher gas puff discharge, presumably because the bootstrap current is suppressed at the higher collisionality. Thus the normalised pressure gradient is constrained at a lower value than the low gas puff cases and the peeling-ballooning boundary is not reached. The slight increase in the ideal ballooning threshold in the final time window may indicate that this plasma is close to having second stable access—if so, that might be having an impact on the pedestal width, but we would need more accurate estimates of the current density to be sure.

Finally, in figure 7 we consider the higher $\beta_N = 1.9$ discharge 87342 which also does not reach the peeling-ballooning boundary. This shows very similar behaviour to discharge 87350. Specifically, the pressure gradient is constrained below, but near to, the ideal MHD ballooning boundary, particularly in the second half of the ELM cycle, indicating a role for KBM physics. Again, there is little sign of any access to second stability. It is interesting to note from figure 1(*d*) that the pedestal width of this discharge does broaden as the ELM is approached, as observed in other, smaller tokamaks.

3.3. Pedestal stability overview

In all 11 low triangularity discharges we have analysed [29] (beyond those described in detail here), if the pedestal has access to second stability, then it reaches the peeling-ballooning boundary at the ELM onset, and the local pressure gradient is constrained below the local ideal ballooning proxy for the KBM (and close to the threshold except at radii where the plasma is in the second stability region). As second stability is predicted to open up, indicating an increase in the KBM threshold, the pedestal pressure gradient rises into it. These results are consistent with KBM and peeling-ballooning playing a dominant role in the physics controlling the pedestal evolution and ELMs. This provides supporting evidence for the physics underlying the EPED model, even though the pedestal width does not always increase monotonically between ELMs at fixed pressure gradient. If the pedestal does not have access to second stability, then the gradients are constrained below, and close to, the predicted ideal ballooning proxy for the KBM threshold as the ELM is approached, but the peeling ballooning boundary is not reached. This then begs the question of what triggers the ELM if the peeling-ballooning boundary is not reached? To begin to address this question, we consider the ELM characteristics in the following section.

4. ELM characteristics

Type I ELMs are widely believed to be a consequence of peeling-ballooning modes. However, in section 3 we presented evidence that indicates the peeling-ballooning stability boundary is not reached in the high gas puff JET-ILW discharges we have considered (consistent with earlier work, which also showed that it *is* reached in high gas puff discharges at lower β_N [23]). In this Section we will seek to shed more light on the underlying physics of the ELM trigger in these cases by characterising their behaviour in more detail, and comparing discharges where the peeling-ballooning boundary is reached at ELM onset to those where it is not.

In figure 8, we show Be II emission integrating over the ten chords which view the inner divertor for the two low gas puff discharges we have analysed, 84797 and 84795, both of which reach the peeling-ballooning boundary at ELM onset. They show the classic sharp rise in emission and slower decay that is characteristic of Type I ELMs. In figure 9 we show the same traces, but for three high gas puff discharges, including shot numbers 87350 and 87342 presented earlier, and now also including a lower $\beta_N = 1.16$ discharge that has lower heating power, 87346; this third discharge is close to the peeling-ballooning stability boundary at ELM onset [23]. Notice that the ELMs in figures 9(*b*) and (*c*) have a different character to the peeling-ballooning triggered ELMs of figure 8—specifically they are more symmetric about the peak in emission and there are shoulders in emission before and after the

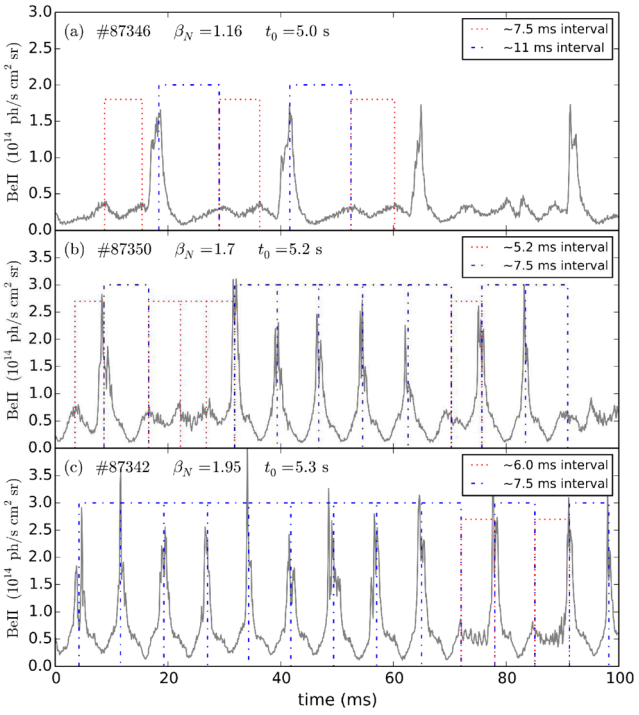

Figure 9. Emission of Be II from the inner divertor, starting at time t_0, showing the ELMs in JET-ILW discharges (*a*) 87346, (*b*) 87350 and (*c*) 87342 all with high gas puff but with different (increasing) β_N. The dotted and dashed boxes denote the time intervals shown in each panel (the different heights of these merely aid distinguishing between them).

ELM spike. Consider first discharge 87350 in figure 9(*b*). At first sight there are two types of periodic behaviour evident in this trace—a low amplitude oscillation and periodic, sharp spikes which are the signatures for ELM-events. The dashed boxes show the period between the peak emission of two consecutive events, independent of whether they are an oscillation or a spike. All the higher blue, dashed boxes have a time period of 7.5 ms and all the lower red, dotted boxes have a time period of 5.2 ms. It is remarkable how regular the events are. Following each spike, the time to the maximum emission of the next event is 7.5 ms, independent of whether it is an oscillation or a spike. Following each oscillation, the time to the next event is 5.2 ms, again independent of whether it is an oscillation or a spike.

A possible interpretation is that the oscillation has a well-defined frequency, and can trigger an ELM as it approaches its maximum amplitude. The resulting crash caused by the ELM takes the plasma slightly longer to recover from, leading to the longer period following an ELM than following an oscillation. If this interpretaton is correct, then figure 9 indicates the coupling between the oscillation and ELMs is β-dependent: at higher β_N, an ELM is triggered at the maximum amplitude of almost every oscillation (figure 9(*c*)), while at lower β_N (figure 9(*a*)) the ELMs do not appear to be paced by the oscillation (which is barely discernable for this discharge) at all. We will see below that this trend with β_N is not observed for the low gas puff discharges analysed, however, so it seems unlikely that β_N is the only control parameter.

To explore this triggering in a more statistical sense, we plot in figure 10 the distribution of ELM periods throughout each of the three high gas puff dicharges analysed. Note how distinct, narrow bands of ELM periods form for discharges 87350 (*c*) and 87342 (*e*)—the lowest band corresponds to an ELM being triggered on the first oscillation; the next band to an ELM triggered after two oscillations, and the highest one after three oscillations. For the lowest β_N case (*a*) there is no sign of bands forming, and little evidence for a correlation between the oscillations and the ELMs. The coupling gets stronger for the higher β_N cases (*c*) and then (*e*). The ELM period probability distributions are shown in figures 10(*b*), (*d*) and (*f*). For the lowest β_N (figure 10(*b*)) there is a broad distribution of relatively long ELM times; for medium β_N (figure 10(*d*)) the ELM periods are significantly shorter, and cluster around the harmonics of the oscillation; for higher β_N (figure 10(*f*)) the majority of ELM periods are in the first harmonic, with a few in the second (indicating almost every oscillation triggers an ELM).

A similar banding of ELM periods was observed in [36, 37] by averaging over many similar discharges. Here we observe such features even within a single discharge.

It is interesting to note that of the three high fuelling discharges analysed, the stronger the apparent coupling between the oscillations and the ELMs (i.e. the more ELMs that fall in the lower band of ELM periods), the further the pedestal is from the peeling-ballooning boundary. This, together with the banding of the ELM periods, provides evidence that (*a*) the oscillations are pacing the ELMs at a frequency which is higher than their natural frequency, and (*b*) the consequent triggering of the ELM before the peeling-ballooning boundary is reached leads to a degraded pedestal and hence reduced confinement. To test this, we have also looked for the oscillation in Be-II emission in the low gas puff discharges which do reach the peeling-ballooning boundary. A careful inspection reveals that the oscillation is there, but the effect on ELM pacing is reduced or completely absent. Indeed, figure 11(*a*) for the higher $\beta_N = 1.7$ low gas puff discharge 84795 shows there is no band at the short ELM period matching that of the oscillations, and there is only a broad range of ELM frequencies at the longer, natural periods. On the other hand, in the lower $\beta_N = 1.3$ low gas puff discharge 84797 there is a clear band of ELMs at period 7–8 ms which matches the oscillation period, but most of the ELMs have a broad distribution across the longer periods. Note, however, that the few (paced) ELMs that follow closely after the preceding ELM in this discharge were not included in the averaged profile data discussed in section 2, so the stability analysis of section 3 for 84797 is pertinent only to the ELMs with longer periods, and not the low period band paced by the oscillation. There is thus consistency in the picture that when the ELMs are not paced by the oscillation, they are triggered at the peeling-ballooning boundary. It is interesting to note that, unlike the high gas puff discharges, in these low gas puff discharges the coupling between the oscillations and ELMs does not apparently increase with β_N.

Our results indicate that it is important to identify the mechanism behind the oscillations in order to improve pedestal performance. We have looked at many discharges,

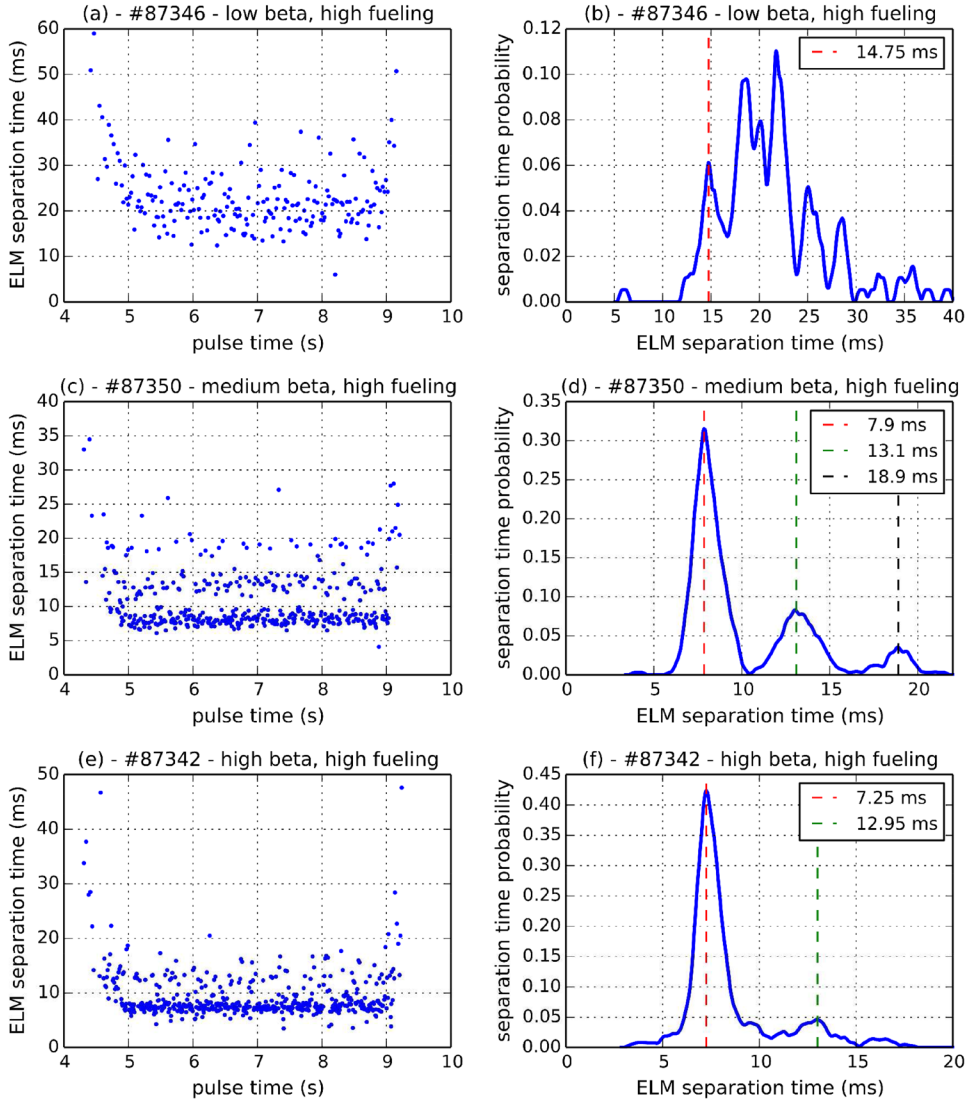

Figure 10. ELM separation time through the pulse for discharges (*a*) 87346, (*c*) 87350 and (*e*) 87342 and their corresponding ELM time probability distributions (*b*), (*d*) and (*f*).

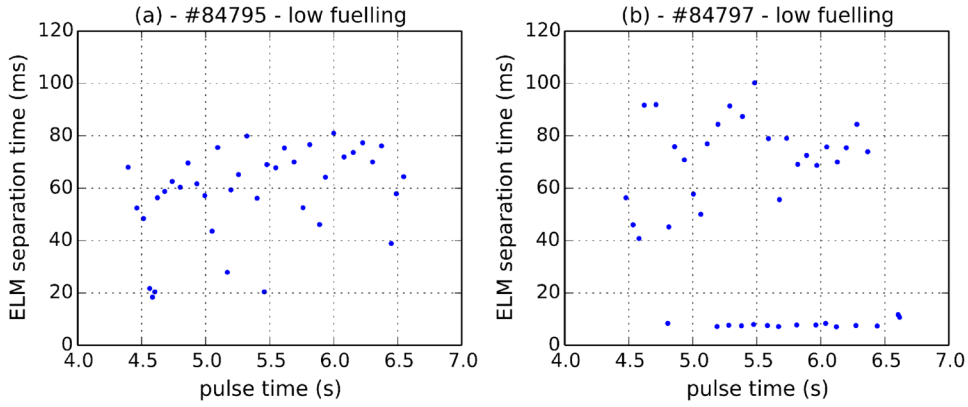

Figure 11. ELM separation times for the low gas puff shots (*a*) 84795 ($\beta_N = 1.7$) and (*b*) 84797 ($\beta_N = 1.3$).

and in most the oscillation starts after several ELMs occur. However, we have found some examples where the oscillation precedes the first ELM (discharge 89238, for example, which has $I_p/B = 2.0/2.2$ MA/T and the outer strike point is on the horizontal target plate inboard of the pumping duct). This provides further evidence that the oscillation is not simply a 'ringing' effect caused by the previous ELM. The oscillations are also seen in other line emissions and all are in phase with each other. Figure 12(*a*) compares the emission for Be-II with D_α, C-III and W-I for the high gas puff discharge 87350 where

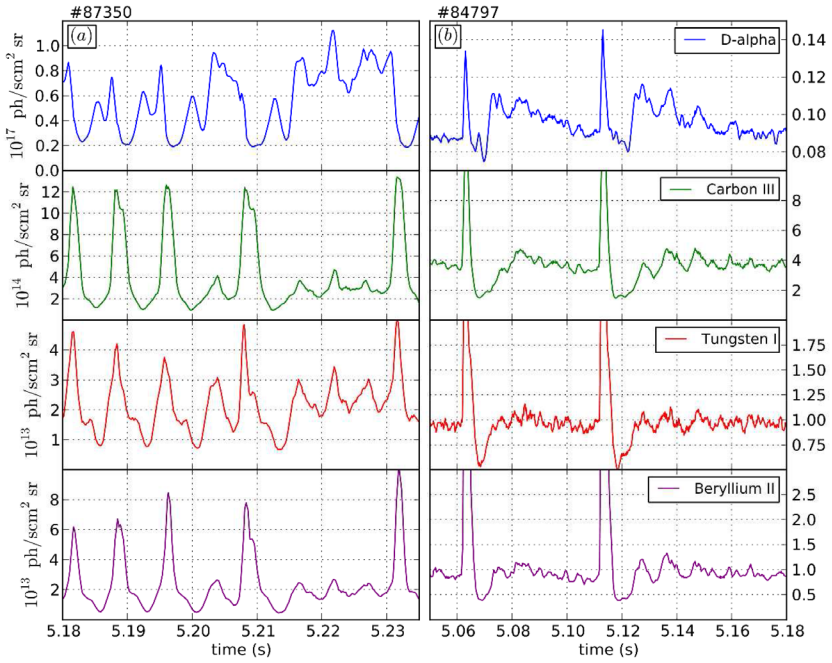

Figure 12. A comparison of emission from lines of D_α, C-III, W-I and Be-II showing that they all exhibit the oscillations in phase for (*a*) the high gas puff discharge 87350 and (*b*) the low gas puff discharge 84797. Note the ELMs in the high gas puff discharge (*a*) correspond to a drop in the D_α emission, rather than the more typical positive spike seen in the low gas puff discharge (*b*).

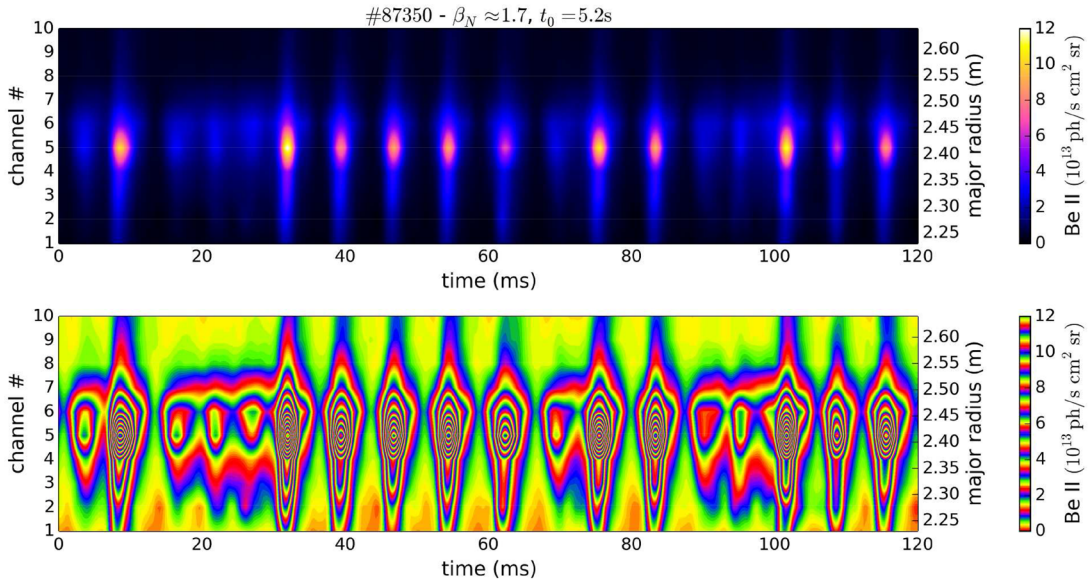

Figure 13. Be II light emission showing clear ELMs and fainter oscillations (upper) and the corresponding prism contour plot, emphasising changes in Be II emission, showing oscillations and ELMs. The channels are viewing the inner divertor region (see right-hand axis for major radius); channels 4–8 view the inner target. Shot 87350—medium β, high gas puff, starting at time $t_0 = 5.2$s.

the oscillations, eg between 5.21 s and 5.23 s are clearly visible in phase in all channels. The ELM spikes also correlate well for the C-III, W-I and Be-II lines. However, note that for the D_α emission, the ELM corresponds to a *reduction* in the emission. Such 'negative ELMs' have been reported earlier, such as in [38]. There it was argued that the inner divertor was in a detached regime between ELMs, where the D_α emission is a consequence of recombination, and then the ELM power flux results in an increase in the number of ionisations per D_α photon, reattachment of the inner divertor, and a consequent decrease in emission. However, between the ELMs in 87350, we see that the D_α rises and falls in phase with the Be II in the oscillations so it is not so clear that this interpretation also holds in this case. This rich divertor physics could shed additional light on the physics of high gas puff discharges, with possible consequences for ELM heat loads (e.g. on ITER) and should be explored further in the future.

To probe the physics of the oscillation in more detail, we compare in figure 13 the Be-II light emission from the 10 channels that view the inner divertor for the medium β_N, high gas puff discharge 87350 (see figure 14). The data we showed in previous figures combines all these channels. Here we can

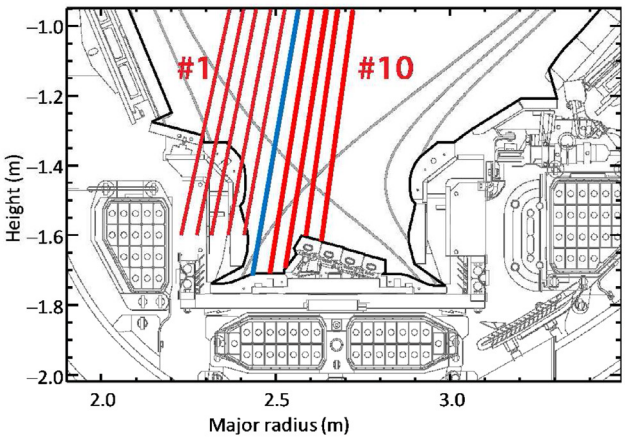

Figure 14. Lines of sight for the Be II emission data shown in figure 13 with channel #1 at the left increasing to channel #10 at the right. Superimposed is the separatrix for shot 87350 at $t = 5.7$s. The blue line denotes the line of sight for channel #6, which is close to the strike point—the peak in emission is between channels #5 and #6.

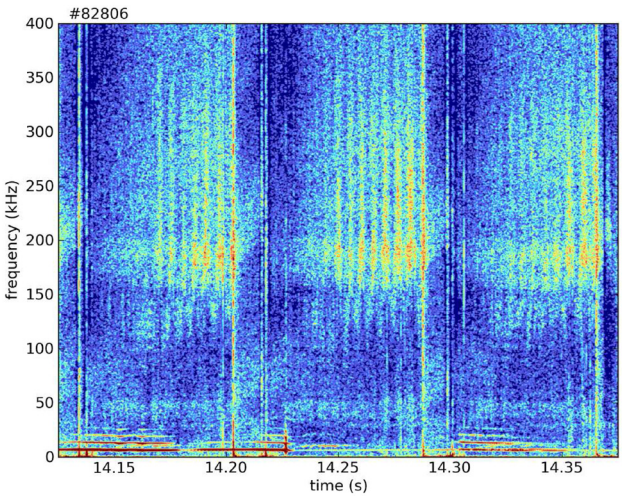

Figure 15. Spectrogram for JET discharge 82806, showing high frequency (150–350 kHz) fluctuations in magnetic field with modulated amplitude occurring between the ELMs (characterised by the events that span all frequencies).

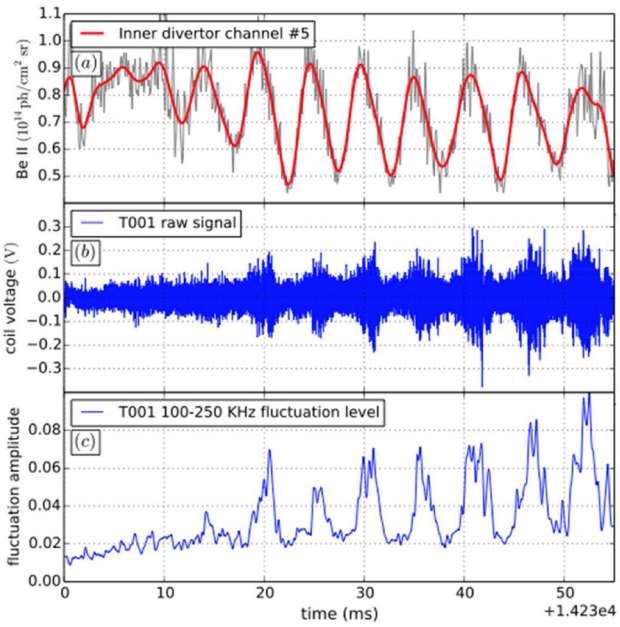

Figure 16. (*a*) Oscillations in the Be II light emission from the inner divertor during an inter-ELM period in discharge 82806 (red curve shows smoothed data) compared to (*b*) Mirnov coil data from the T001 coil positioned outboard of the plasma above the mid-plane, and (*c*) fluctuation amplitude integrating over the 100–250 kHz frequency range.

see that the oscillation, more clearly visible in the lower prism plot, is strongest in those channels which directly view the divertor target (channels 4–8), while the ELM is seen across all channels. Viewing the outer divertor yields the same result, exactly in phase with the inner divertor. There is a similar picture from the other views—only those channels viewing the divertor target see the oscillation in Be-II, but the ELM is seen in all channels. The data in figure 13 seem to rule out a significant displacement of the whole plasma as a possible mechanism for the oscillation in Be II emission. Specifically, note for all channels 3–7, the emission rises and falls at the same time, rather than the emission peak migrating from one channel to another, as might be expected if the plasma (strike-point) is moving. This suggests that the Be-II oscillation is due to a pulse of heat and particles that travels along the scrape-off layer, arriving at the two divertor targets at the same time, and creating a plume of Be that results in the observed emission there. If so, we are not directly observing the origin of the oscillation by viewing the Be-II emission—rather, a symptom of it. An alternative explanation is provided in [39] related to an instability of the detachment front, as follows. Impurities released from the target plate strike point enter the divertor region, radiate and cool the plasma there. The divertor then detaches, reducing the heat flux to the target plates so that less impurities are released. The impurities in the divertor then diminish, radiation falls, the divertor plasma heats back up and re-attaches for the process to cyclicly repeat.

To understand whether the fundamental drive for the Be II oscillation originates from an instability of the core/pedestal, we have studied Mirnov coil data, which reveals high frequency activity across a range 150–350 kHz with a modulated amplitude. Furthermore, for all the coils we have looked at, over a range of poloidal and toroidal locations, this modulation of the amplitude is in phase with the oscillations in the Be-II emission. Before we consider our data set, we show in figures 15 and 16 a particularly striking example from the discharge 82806 ($I_p/B = 2.5/2.65$ MA/T, higher triangularity $\delta = 0.4$ and the outer strike point is on the horizontal target plate inboard of the pumping duct); this is convenient because of the larger number of oscillations that occur between ELMs. This discharge is one of a series discussed in [22]. Figure 16(*a*) shows the oscillations in the Be-II emission compared to the Mirnov coil data in figure 16(*b*). This coil is positioned outboard of the plasma, above the mid-plane, but all coils we have looked at, across a range of poloidal and toroidal angles, show the same behaviour, with the modulation in the amplitude all in phase with each other. The high frequency oscillations are broad-band, typically in the range 150–350 kHz

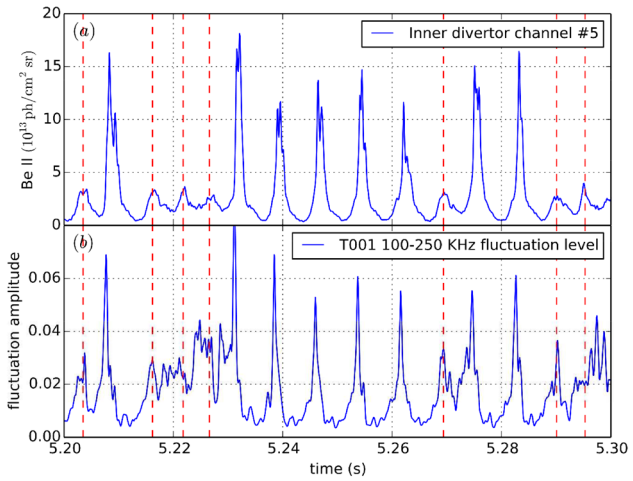

Figure 17. (*a*) Be II light emission in discharge 87350 compared to (*b*) the magnetic field fluctuation amplitude in the 100–250 kHz range. The vertical dashed lines align with the peak of the oscillations in Be II emission. The magnetics data is taken from the T001 Mirnov coil positioned outboard of the plasma above the mid-plane.

(see figure 15), modulated in phase with the Be II emission. In figure 16(*c*) we show the magnetic fluctuation amplitude, which we have determined by isolating the high-frequency activity using a 100–250 kHz band-pass filter and then calculating the analytic signal amplitude, which can be obtained using the Hilbert transform [40]. This yields the instantaneous amplitude of the signal as a function of time. The analytic signal amplitude time-series has been smoothed with a 0.1 ms Gaussian moving average to yield the mean fluctuation level over time shown. Note that in this case, the Mirnov signal falls to background levels around the minima in the Be-II emission, indicating that the activity is switching off between successive bursts.

In figure 17 we compare the Be II emission with the fluctuation amplitude derived from the same Mirnov coil as studied in figure 16, but this time for our high gas puff, medium β_N discharge 87350. Again we see enhanced high frequency magnetic fluctuations associated with the oscillation in the Be-II emission. There is a difference between this discharge and that of figure 16 however, in that the magnetic signal does not always fall to background levels between oscillations, but stays high relative to the background until the onset of the ELM.

For the discharges studied in [36, 37], it was postulated that the ELMs might be paced by an oscillation of the plasma position caused by the control system. Such an explanation would help to explain why the oscillation period is so constant across many discharges. However, it is difficult to explain the high frequency magnetic activity in terms of bulk motion of the plasma and, as mentioned above, it is difficult to reconcile a bulk plasma motion with the Be-II emission across the channels viewing the inner divertor (figure 13). Also, one would expect the amplitude of the Mirnov activity of coils above and below the mid-plane to be out of phase if the plasma were oscillating up and down, and we see them very much in phase. A rapidly rotating, high n, filamentary magnetic structure near the plasma edge that repetitively pushes out and relaxes back to provide the amplitude modulation seems a more likely explanation, as we discuss in the following Section.

5. Conclusions

We have considered the pedestal evolution and ELM characteristics of JET-ILW low triangularity discharges. We have found that for low gas puff the pedestal often has second stability access to ideal MHD ballooning modes and, as this opens up, the pedestal pressure gradient rapidly rises to track the increasing instability threshold. This provides strong evidence that the KBM is constraining the inter-ELM evolution in these pedestals, but not at a fixed pressure gradient. Furthermore, we have argued that the pedestal width evolution is influenced by the region of edge plasma that has access to second stability, and this can lead to complex dynamics—including a reduction in the pedestal width when only a small part of the pedestal penetrates into the second stability region. The regions of plasma that are second-stable to $n = \infty$ ideal MHD are also expected to have enhanced stability to the KBM [24], so it is possible that other microinstabilities control the pedestal transport in these regions. Our local gyrokinetic stability calculations for discharge 84795 confirm the absence of the local KBM in those second stable regions of the pedestal. Three ion-scale instabilities have been identified, including one with characteristics of a hybrid TEM/KBM [35], as well as electron-scale electron-temperature gradient modes. It is important to note, however, that global effects are known to destabilise KBMs in the second stability regime [8], so the local analysis is unlikely to be sufficient in such situations. Furthermore, high n ideal MHD calculations [7, 28, 29] indicate that the kink/peeling drive can become important due to the high bootstrap current, and this also restricts access to the second stability regime (but at higher pressure gradient than the first stability boundary). The kink drive is ordered out of standard gyrokinetics, so testing the influence of this physics on kinetic KBM stability thresholds requires further theoretical developments.

Of all the 11 discharges analysed across all three gas puff levels [29], if the pedestal accesses second stability, it reaches the peeling-ballooning boundary at the onset of the ELM. In these cases, there is consistency with the physics basis of the EPED model—the pressure gradient tracks the KBM threshold (modified as appropriate, e.g. for global effects), which is not constant between ELMs, and the ELM is triggered by a peeling-ballooning mode. The low gas puff discharges analysed fall into this category.

If the pedestal does not have second stability access it is often some way short of the peeling-ballooning boundary at the time of the ELM, even though the gradient is close to the ideal ballooning KBM threshold proxy. In those cases we have identified an oscillation in the Be-II emission that seems to pace the ELMs, triggering them at a higher frequency and lower pressure gradient than required for intermediate n peeling-ballooning instability. Thus we expect the measured pedestal height in these cases to be degraded somewhat

compared to the EPED model predictions, leading to reduced confinement.

It has recently been proposed that JET is sitting at a transition point in normalised ion Larmor radius, ρ_*, below which shear flow is ineffective at suppressing the ion temperature gradient mode and the associated transport. Reducing ρ_* through this transition point would also lead to a degraded pedestal and reduced overall confinement [41]. It is clearly important in extrapolating to ITER that we identify which is the dominant effect and, if the effect of the oscillation on ELMs is key, we need to identify its origin and seek ways to eliminate it, or influence its ability to trigger ELMs and consequent pedestal collapse.

Speculating on the origin of the oscillation, we have shown that (1) the plasma pressure gradient is close to the ideal MHD ballooning mode proxy for the KBM, and (2) the oscillations have a clear 150–350 kHz magnetic signal observed in Mirnov coil data, with an amplitude that is modulated in phase with the oscillations in the Be-II emission. A possibility we propose, therefore, is that the oscillation we are observing is a non-linear consequence of the KBM. Non-linear theory has previously shown that ideal MHD ballooning modes can erupt explosively even without the kink/peeling drive [42], and this provides a possible model for ELM dynamics. A more recent theory has shown that as the first stability boundary is approached, the ballooning instability can result in a finite displacement of plasma filaments rather than an eruption [43]; these hot filaments would be expected to drain diffusively into the cooler surrounding plasma to remove the free energy driving them so that they subsequently relax back towards their initial position, for the process to then repeat, cyclically. This could be consistent with the observed Mirnov activity, with the high frequency corresponding to the multiple fine filaments rotating past the coils, and the modulation in the amplitude associated with the filaments pushing out and relaxing back. We cannot yet quantify the theoretical conditions required for a ballooning mode to provide a benign displacement (the oscillation?), and when it drives an explosive eruption (the ELM?), so it is difficult to comment more quantitatively at this stage; however a possibility to explore further in the future is that we are observing an evolution from an oscillatory state to an explosive state as the plasma approaches and then exceeds the linear stability boundary.

There is a second possible explanation related to generic linear ballooning theory (i.e. not just a property of MHD) in the presence of sheared toroidal flows. Because the rational surfaces then rotate relative to each other, the poloidal angle where individual poloidal Fourier harmonics centered on their respective rational surfaces constructively interfere to form the ballooning modes evolves in time. When the peak in amplitude is on the outboard side, the growth rate is typically maximum, and while it is on the inboard side it is typically minimum (and can even damp). This is a Floquet mode, which periodically grows and decays with a well-defined period related to the ratio of flow shear to magnetic shear [44, 45]. This physics could provide the basis for a model for the evolution of the oscillations and then, perhaps, the ELM as the profiles (e.g. flow shear) evolve through a critical point [45]. Tests would require careful measurements of flow and magnetic shear in the vicinity of the mode (which are challenging), as well as more accurate, quantitative non-linear models.

The above two possibilities are related to pedestal physics, with a ballooning-type instability increasing transport into the SOL, enhancing the interaction with the divertor target plates and releasing the Be which we observe through the Be II emission. Another possibility proposed in [39] is that the oscillation is related to the release of impurities from the target plates which radiate in the divertor, cooling the plasma there and causing detachment. The resulting reduction in target plate interaction reduces the impurity influx, lowering the radiation, re-heating the divertor plasma, causing it to re-attach and the cycle to repeat. It remains to be understood how this mechanism might relate to the observed magnetic signal and the ELM trigger, but a possibility is the impact of detachment on the pedestal profiles and hence stability (like the mechanisms discussed in [25], for example).

While the role of the oscillation in the JET pedestal dynamics remains uncertain, there is a clear practical message suggested by this study—avoiding the oscillation and maximising the region of edge plasma that has access to second stability will help to optimise the pedestal and therefore confinement. The relationship between current density and pressure gradient is important for navigating under the nose of the *s*-alpha diagram to access second stability. Plasma shaping plays a role here, so an important direction for future research is to repeat this study in high triangularity discharges.

Acknowledgments

The authors are grateful for the detailed comments and suggestions from J. Hillesheim during the preparation of this paper. This work has been carried out within the framework of the EUROfusion Consortium and has received funding from the Euratom research and training programme 2014-2018 under grant agreement No 633053. The views and opinions expressed herein do not necessarily reflect those of the European Commission. We also acknowledge support from the EPSRC grants EP/L01663X/1 and EP/K504178/1, which fund the EPSRC Centre for Doctoral Training in the Science and Technology of Fusion Energy. The authors acknowledge access to the EUROfusion High Performance Computer (Marconi-Fusion) through EUROfusion and to the ARCHER computing service through the Plasma HEC Consortium EPSRC grant number EP/L000237/1.

To obtain further information about the data and models underlying this paper please contact publications.officer@euro-fusion.org.

Appendix. Peeling-ballooning stability methodology

This appendix provides a summary of the procedure for assessing the peeling-ballooning stability of the JET-ILW pedestals. A more detailed discussion can be found in [29].

Electron density and temperature profiles are measured using the JET HRTS system throughout the discharge and binned into one of five equally spaced inter-ELM time windows. The average profile for each window is then fitted using a modified tanh function, with parameters that characterise the pedestal height, the separatrix value, the position of the centre of the edge transport barrier, the gradient in the pedestal and the gradient in the core. Electron and ion temperatures are assumed to be equal, and the full pressure calculated for a given average effective charge, Z_{eff}, in the pedestal. This enables the equilibrium to be reconstructed using HELENA [30], employing the Koh–Chang model for the pedestal bootstrap current [46].

To avoid non-robust weakly growing peeling modes, 'marginal stability' is defined to be the point where the growth rate $\gamma = 0.03\ \omega_{\mathrm{A}}$, where ω_{A} is the Alfven frequency. Five equilibria are generated using the HELENA code—the operating point; two at lower pedestal width, and two at greater pedestal width. These equilibria are generated by adjusting the widths of temperature and density pedestals, while keeping the pedestal heights and the separatrix values fixed. For each of the five pedestal widths, the pedestal height is steadily increased, calculating new equilibria using the self-consistent bootstrap current. At each pedestal height the stability is explored using ELITE [27, 28] up to toroidal mode number, $n = 70$, to identify the marginally stable pedestal height. This then defines the marginal stability curve in pedestal height versus width, which are both defined in terms of total pressure.

ORCID iDs

H.R. Wilson https://orcid.org/0000-0003-3333-7470
B. Lipschultz https://orcid.org/0000-0001-5968-3684

References

[1] Wagner F. *et al* 1982 *Phys. Rev. Lett.* **49** 1408
[2] Snyder P.B. *et al* 2009 *Phys. Plasmas* **16** 056118
[3] Snyder P.B. *et al* 2011 *Nucl. Fusion* **51** 103016
[4] Connor J.W. *et al* 1998 *Phys. Plasmas* **5** 2687
[5] Wilson H.R. *et al* 1999 *Phys. Plasmas* **6** 1925
[6] Snyder P.B. and Hammett G.W. 2001 *Phys. Plasmas* **8** 744
[7] Wilson H.R. and Miller R.L. 1999 *Phys. Plasmas* **6** 873
[8] Saarelma S. *et al* 2017 *Plasma Phys. Control. Fusion* **59** 064001
[9] Groebner R.J. and Osborne T.H. 1998 *Phys. Plasmas* **5** 1800
[10] Urano H. *et al* 2008 *Nucl. Fusion* **48** 045008
[11] Kirk A. *et al* 2009 *Plasma Phys. Control. Fusion* **51** 065016
[12] Maggi C.F. *et al* 2017 *Nucl. Fusion* **57** 116012
[13] Dickinson D. *et al* 2012 *Phys. Rev. Lett.* **108** 135002
[14] Groebner R.J. *et al* 2013 *Nucl. Fusion* **53** 093024
[15] Snyder P.B. *et al* 2012 *Phys. Plasmas* **19** 056115
[16] Diallo A. *et al* 2014 *Phys. Rev. Lett.* **112** 115001
[17] Diallo A. *et al* 2015 *Phys. Plasmas* **22** 056111
[18] Beurskens M. *et al* 2014 *Nucl. Fusion* **54** 043001
[19] Frassinetti L. *et al* 2017 *Plasma Phys. Control. Fusion* **59** 014014
[20] Leyland M.J. *et al* 2013 *Nucl. Fusion* **53** 083028
[21] Leyland M.J. *et al* 2015 *Nucl. Fusion* **55** 013019
[22] Giroud C. *et al* 2013 *Nucl. Fusion* **53** 113025
[23] Maggi C.F. *et al* 2015 *Nucl. Fusion* **55** 113031
[24] Saarelma S. *et al* 2013 *Nucl. Fusion* **53** 123012
[25] Dunne M.G. *et al* 2017 *Plasma Phys. Control. Fusion* **59** 014017
[26] Frassinetti L. *et al* 2012 *Rev. Sci. Instrum.* **83** 013506
[27] Wilson H.R. *et al* 2002 *Phys. Plasmas* **9** 1277
[28] Snyder P.B. *et al* 2002 *Phys. Plasmas* **9** 2037
[29] Lunniss A.E. 2017 Modelling eruptions and edge stability in Tokamak plasmas *PhD Thesis* University of York (http://etheses.whiterose.ac.uk/16638)
[30] Huysmans G.T.A., Goedbloed J.P. and Kerner W. 1991 *Proc. CP90 Conf. on Computing Physics (Amsterdam, The Netherlands)* (Singapore: World Scientific) p 371
[31] Bishop C.M. 1986 *Nucl. Fusion* **26** 1063
[32] Dickinson D. *et al* 2013 *Plasma Phys. Control. Fusion* **55** 074006
[33] Hillesheim J.C. *et al* 2015 *Plasma Phys. Control. Fusion* **58** 014020
[34] Kotschenreuther M., Rewoldt G. and Tang W.M. 1995 *Comput. Phys. Commun.* **88** 128
[35] Guttenfelder W. *et al* 2013 *Nucl. Fusion* **53** 093022
[36] Webster A.J. *et al* 2014 *Plasma Phys. Control. Fusion* **56** 075017
[37] Webster A.J. *et al* 2015 *Phys. Plasmas* **22** 082501
[38] Loarte A. *et al* 1998 *Nucl. Fusion* **38** 331
[39] Field A.R. *et al* 2017 *Nucl. Fusion* submitted
[40] Feldman M. 2011 *Mech. Syst. Signal Process.* **25** 735
[41] Kotschenreuther M. *et al* 2017 *Nucl. Fusion* **57** 064001
[42] Wilson H.R. and Cowley S.C. 2004 *Phys. Rev. Lett.* **92** 175006
[43] Ham C.J., Cowley S.C., Brochard G. and Wilson H.R. 2016 *Phys. Rev. Lett.* **116** 235001
[44] Taylor J.B. and Wilson H.R. 1996 *Plasma Phys. Control. Fusion* **38** 1999
[45] Bokshi A., Dickinson D., Roach C.M. and Wilson H.R. 2016 *Plasma Phys. Control. Fusion* **58** 075011
[46] Koh S. *et al* 2012 *Phys. Plasmas* **19** 072505